Marie Skłodowska Curie Action

WINDMILL

Machine Learning for Wireless Communications

H2020-MSCA-ITN-ETN

Grant Agreement Number: 813999

WP4–Prediction Schemes and Anticipatory Optimization for Fast-Varying Processes.

D4.1–Synthetic Data Generation for Machine Learning of Fast-Varying Wireless Processes

"Original Title: Massive-MIMO mmWave Channel Model and System Simulator Description"

Contractual Delivery Date:	August 31, 2020
Actual Delivery Date:	July 22, 2020
Responsible Beneficiary:	AALTO
Contributing Beneficiaries:	EUROCOM, AAU
Dissemination Level:	Public
Version:	Draft

PROPRIETARY RIGHTS STATEMENT

This project has received funding from the European Union's Horizon 2020 research and innovation programme under the Marie Skłodowska-Curie grant agreement No 813999.

PROPRIETARY RIGHTS STATEMENT
This project has received funding from the European Union's Horizon 2020 research and innovation programme under the Marie Skłodowska-Curie grant agreement No 813999.

Document Information

Document ID:	WP4/D4.1
Version Date:	August 31, 2020
Total Number of Pages:	53
Abstract:	Machine Learning (ML) approaches have attracted researchers in wireless communications to employ and develop ML algorithms in order to exploit information about the radio channels. However, ML methods are data hungry and to obtain reliable results huge amount of real world measurements are needed. This problem can be circumvented by generating authentic synthetic data which mimics the behavior of realistic data. To do so, accurate simulators need to be designed and created based on mathematical models and measured data. In this report, synthetic data use cases in three different applications are briefly discussed. An overview of channel models appropriate for Fifth Generation and Beyong Fifth Generation (B5G) systems is given. Channel model characteristics including path loss, Large-Scale Fading and Small-Scale Fading models, are discussed, and differences of Millimeter-Wave and microwave models are explained. The QUAsi Deterministic RadIo channel GenerAtor (QuaDRiGa) and ray-tracing channel simulators are discussed. For ML use cases where radio characteristics are to be predicted from traces of user channel measurements, spatial consistency of the channel model is paramount. Spatial consistency of channels generated in QuaDRiGa is investigated here. As an example use of spatially consistent channel models, channels generated by a ray-tracing model are used in a channel charting based algorithm for handowver, and the performance of the system is evaluated. One of the B5G developments that is often highlighted is the integration of wireless communication and radio sensing. The potential of communication-sensing integration of Large Intelligent Surfaces (LIS) is still under development. By treating a LIS as a radio image of the environment, sensing techniques that leverage the tools of image processing and computer vision combined with machine learning can be undertaken.

Authors

Full name	Beneficiary/ Organisation	e-mail	Role
Parham Kazemi	AALTO	parham.kazemi@aalto.fi	Contributor, editor
Matteo Zecchin	EUROCOM	zecchin@eurecom.fr	Contributor
Cristian J. Vaca Rubio	AAU	cjvr@es.aau.dk	Contributor

Reviewers

Full name	Beneficiary/ Organisation	e-mail	Date
Olav Tirkkonen	AALTO	olav.tirkkonen@aalto.fi	August 31, 2020
Hanan Al-Tous	AALTO	hanan.al-tous@aalto.fi	August 31, 2020
David Gesbert	EUROCOM	david.gesbert@eurecom.fr	August 31, 2020

Version history

Version	Date	Comments
v0.1	August 26, 2020	Draft without abstract and conclusions
v0.2	August 28, 2020	Conclusions and abstract added
v0.3	August 31, 2020	Formatting, incorporating review comments
v1.0	August 31, 2020	Submitted version

Executive Summary

Table of Contents

List of Figures

List of Acronyms and Abbreviations

3GPP 3rd Generation Partnership Project

5G Fifth Generation

A_{max} Maximum Attenuation Power

A''_{dB} 3D Antenna Radiation Power

AoA Azimuth angle-of-Arrival

AoD Azimuth angle-of-Departure

ASA Azimuth Spread of Arrival angles

BS Base Station

B5G Beyong Fifth Generation

CC Channel Chart

CCNCH Channel Chart-based-Network-Centric-Handover

CIR Channel Impulse Response

CMD Collinearity Matrix Distance

CSI Channel state Information

DM Decision Maker

DNN Deep Neural Network

DS Dealy Spread

EoA Elevation angle-of-Arrival

EoD Elevation angle-of-Departure

Gbps Gigabit-per-second

GNSS Global Navigation Satellite System

GO Geometrical Optics

GPS Global Positioning System

GPR Gaussian Process Regression

GSCM Geometry-based Stochastic Channel Model

HPBW Half Power Beam Width

HO Handover

HMIMO Holographic MIMO

i.i.d Independent and Identically Distributed

IoT Internet of Things

LIS Large Intelligent Surfaces

LSF Large-Scale Fading

LoS Line of Sight

ML Machine Learning

mMTC massive Machine Type Communications

mMIMO Massive-MIMO

mm-Wave Millimeter-Wave

MIMO Multi Input Multi Output

MPC Multi-Path Components

MPCC Multi-Point Channel Chart

MSE Mean Squared Error

NN Neural Networks

NLoS Non Line of Sight

NR New Radio

O2I Outdoor to Indoor

OFDM Orthogonal Frequency Division Mutiplixing

QD Quasi Deterministic

QuaDRiGa QUAsi Deterministic RadIo channel GenerAtor

RF Radio Frequency

RRM Radio Resource Management

RX Receiver

RSS Received Signal Strength

RMS Root Mean Square

RMSE Root Mean Square Error

RMa Rural Macro

SLA_V Side-Lobe Attenuation in Vertical direction

SNR Signal-to-Noise Ratio

SSF Small-Scale Fading

SOS Sum of the Sinusoids

SVM Support Vector Machine

TDL Tapped Delay Line

TX Transmitter

UAV Unmanned Aerial Vehicle

UCA Uniform Circular Array

UE User Equipment

ULA Uniform Linear Array

UMa Urban Macro

UMi Urban Micro

UPA Uniform Planer Array

URLL Ultra Reliable and Low Latency

UTD Uniform Theory of Diffraction

V2V Vehicle to Vehicle

Report Organization In this report, we consider Millimeter-Wave (mm-Wave) channel models and provide two different system simulators for Massive-MIMO (mMIMO) mm-Wave systems. In Section 1, the role of synthetic data in wireless communication research field is explored and three different applications powered by machine learning are introduced. In Section 2, basic concepts and models of the wireless channels are discussed. Also, mm-Wave channel model, basic principals and the differences between microwave and mm-Wave channels are discussed. In Sections 3 and 4, QUAsi Deterministic RadIo channel GenerAtor (QuaDRiGa) and Ray-tracing models are presented and simulation results of a few different scenarios are presented. In Section 5 examples of channel generation using different models are presented. Finally, in Section 6, conclusions are drawn.

Notation We adopt the following notation: matrices and vectors are set in upper and lower boldface, receptively. $(\cdot)^T$, $(\cdot)^*$, $(\cdot)^H$, $|\cdot|$, $||\cdot||_p$ denote the transpose, the conjugate, the Hermitian, the absolute value, and the p-norm, respectively. $\mathrm{Tr}(\mathbf{A})$ denotes the trace of matrix $\mathbf{A}$. Calligraphic letters denote sets, e.g., $\mathcal{G}$, and $|\mathcal{G}|$ denotes the cardinality of $\mathcal{G}$. $\mathbb{R}_+$ is the set of non-negative real number, $\mathbb{C}$ is the set of complex numbers, and $\mathbb{C}^{N\times M}$ is the space of $N \times M$ matrices. $\mathbb{E}[\cdot]$ denotes expectation. $\mathrm{vec}(\mathbf{X})$ denotes the vector obtained of stacking the columns of matrix $\mathbf{X}$ on top of one another.

1. Synthetic Data Generation for WP4 Research Tasks

During the past four decades, wireless communications have experienced four generations of technologies and the latest, Fifth Generation (5G) is here, the standard is ready, and products are being sold. One key challenge is the development of extremely sophisticated wireless systems that hold many promises such as: ever-higher data rates, networks of Unmanned Aerial Vehicle (UAV), massive Machine Type Communications (mMTC) and autonomous cars. The range of service requirements is expected to be very diverse. A dramatic boost will come with the introduction of Internet of Things (IoT) systems. The antenna densification at the network side comes as a natural mirroring solution to absorb the upcoming traffic surge while responding to the need for high data rates. The need for high data rates will continue to be one of the drivers of the evolution of wireless networks, especially with emerging bandwidth-hungry applications such as virtual reality.

The design approaches used in current wireless systems rely on mathematical models, developed to represent their actual fundamental physical behavior. These models are used to formulate specific performance optimization problems via carefully constructed objective functions. This approach is not easily amenable to encompassing a multitude of dense, interconnected networks obeying different performance metrics. Due to the shortcomings of the optimization/management tools and the simple models employed in the current wireless systems, the future generation of wireless networks is in the need of new tools that can scale with their extreme levels of complexity and drive their evolution towards the promised performance level.

Future wireless networks will be a formidable sensing and data collection system. While data from user devices or sensing networks is used to extract contextual information, wireless networks offer the distinctive opportunity to gather wireless channel measurements. Thanks to the antenna densification at both the device and network side, those measurements provide a very fine sampling of the space, rich in information about the radio channels, the traffic patterns or active wireless devices. Thus, huge volumes of valuable data are produced by the network and Users which could be leveraged by ML tools.

Machine Learning is a versatile tool that does not require detailed specification of a mathematical model based on the physical properties of the system [1]. Rather, the main principle behind ML is to learn from observations, examples or experience, and build workable models of manageable complexity and algorithms that make decisions and predictions. In this regard, the massive data flows in future communication networks can be seen as an asset rather than a burden. Additionally, ML facilitates automation, thereby decreasing the maintenance costs and assisting the deployment of robotic networks (e.g. networks of UAVs or autonomous cars).

The objective in Work Package 4 (WP4) is to develop ML methods for the physical layer in massive multi-antenna systems. One goal is to learn and anticipate spatio-temporal features related to the wireless channel in multiuser multi-antenna networks [1]. The radio channel poses a tough challenge to conventional ML methods due to its fast variability. Conventional physical layer designs are based on reactive estimation of the channel, and optimization in feedback loops. For future systems with extreme dimensionality, proactive methods are needed, based on anticipatory estimation of the radio channel. Tools will be developed to acquire different levels of information about the channel. Radio maps describing channel characteristics in mMIMO systems will be considered, leading to anticipatory optimization of user-specific spectral resources. Distributed and centralized processing will be addressed, in particular distributed channel estimation and multi-user beamforming in mMIMO, multi-cell, connected vehicles.

Collecting labeled data which is a necessity for ML based models is still a consideration in wireless communications community. Obtaining a real data set is expensive and limited to the measurement setup. Therefore, results are difficult to generalize to other radio environments, or a different radio frequencies. Since manual labeling which is mainly performed by humans is costly and drastically time consuming, synthetic data generation is a viable alternative for generating training data for wireless ML tasks. Synthetic data can be easily generated based on previously evaluated and (experimentally) verified models. As mentioned, providing realistic data on large scale is not feasible from a business perspective. Also, most companies pioneering wireless technologies have strict policies on sharing data which hinders research performed from outside of such companies.

One approach is to generate synthetic data that have similar characteristics to the original data but the value of not requiring direct measurement. By so doing, the privacy constraints of companies on data is circumvented and a vast set of assumptions could be considered. The challenging part of generating synthetic data is capturing statistical and structural characteristics of the real data. In addition, tradeoffs between computational complexity, run time, and synthetic data level of statistical accuracy must be considered.

Therefore, in this work package, synthetic channels will be used to generate data for physical layer machine learning problems. The problems of wireless channel prediction for beam and cell handover management, collaborative deep learning for distributed power control, and predictive machine learning for multiuser beamforming will be addressed. When dissecting these problems we find that for distributed power control, discussed in section 1.2, the characteristics to learn are not seriously affected by the details of the channel model. For prediction of beams, and handovers, discussed in section 1.1 and for exploiting Channel state Information (CSI) in LIS communications in section 1.3, spatial consistency of channel models is crucial. Spatial consistency has conventionally not been an issue in channel models used for wireless system modeling, only recently has it been raised to a desired feature of models. Moreover, the main avenue for 5G and beyond systems to provide added value over 4G is in the possibility to use mm-Wave channels. As a consequence, in the coming chapters we shall concentrate on spatially consistent channel models for mm-Wave systems.

Note: Originally, the planned title of this deliverable was “Massive-MIMO mm-Wave Channel Model and System Simulator Description”. The title was changed to the current one better to reflect the diverse requirements on synthetic data generation of the research tasks of WP4. Much of the content of sections 2, 3 and 4 fall under the original title.”

1.1. Multipoint Channel Charting for Wireless Channel Prediction

Future wireless communication systems must sustain a massive increase in traffic volumes, number of terminals, and reliability/latency requirements [2]. In order to cope with these challenges, researchers have proposed a range of new technologies that improve spectral efficiency through mMIMO, increase bandwidth by harnessing mm-Wave bands for mobile communication, and rely on an extreme densification of network elements. While the advantages of these emerging technologies are glaring, they entail severe practical challenges. Mobility, in particular, poses problems for dense small-cell networks [3], as well as for mMIMO and mm-Wave networks, which provide extremely fine-grained angular separation.

To efficiently manage a mMIMO network, and to perform cognitive networking tasks, the network states which include the spatial distribution and trajectories of the UEs, neighborhood relationships among the UEs, and Handover (HO) boundaries among neighboring cells need to be estimated. A novel ML framework called Channel Chart (CC) based on the massive amounts of CSI available at the base stations is proposed for a single-cell Multi Input Multi Output (MIMO) system in [2]. CC applies unsupervised ML techniques to create a radio map of the cell served by the BS, which preserves the neighborhood relations of UEs, using features that characterize the Large-Scale Fading (LSF) effects of the channel. The obtained CC can be used for local Radio Resource Management (RRM) in the cell.

However, cell edge UEs may not be accurately located in the chart due to their low SNR at the cell edge. In [4], a MPCC framework is proposed to support advanced multicell RRM and to accurately map cell edge UEs. First, each BS generates its own dissimilarity matrix between the users it can decode; then, the dissimilarity matrices are fused and used to construct the MPCC. A CC is constructed using an unsupervised ML framework that processes the dissimilarity matrix, manifold learning is used to dimensionally reduce the CSI feature space. The block diagram of principals of MPCC is shown in Figure 1.1. The trustworthiness and continuity measures show that the proposed MPCC is capable to preserve the neighborhood structure between UEs in the network. MPCC-based approach entails more computational efforts compared to other approach at the BSs to compute the dissimilarity matrix between the UEs seen by the same BS [5].

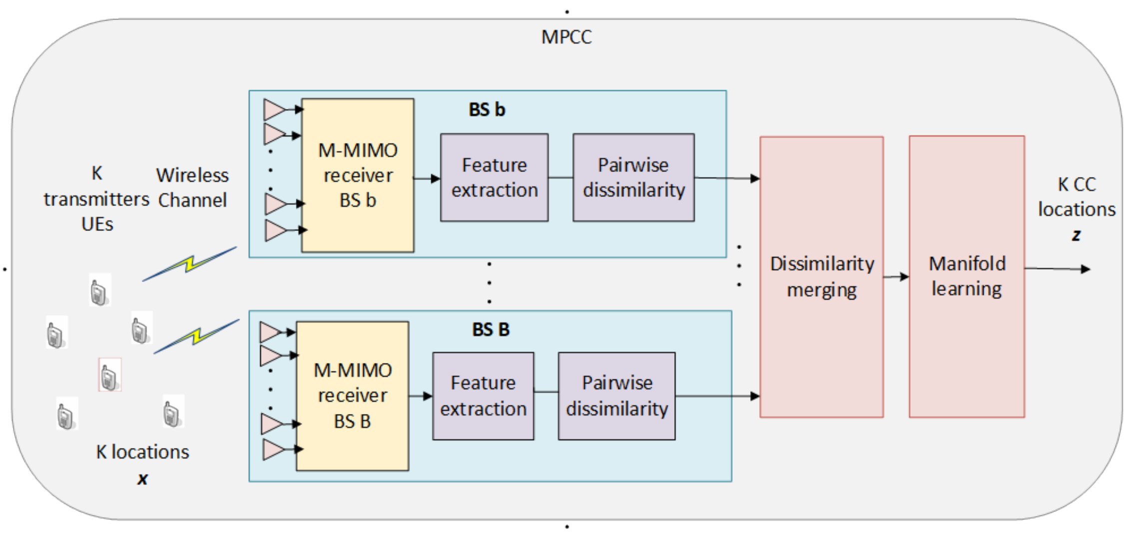

Figure 1.1: The principals of MPCC.

SNR prediction of neighboring BSs is exploited based on relative locations, such as CC. This is an example of data-driven wireless communication problem. SNR prediction based on CC is an attractive approach since neither the physical location information nor the downlink channel measurement at the UE terminal are needed to predict the SNR of a neighboring

BS. HO algorithms can be designed based on the predicted neighboring BS SNR, reducing power consumed at the UE, and signaling overhead. Therefor, machine learning algorithms could be exploited to predict the SNR of a user transmitting at a neighboring BS in a mMIMO cellular system. This information is needed for HO decisions for mobile users. For SNR prediction, only uplink channel characteristics of users, measured in a serving cell, are used. Here, we learn an annotation of the CC in terms of neighboring BS signal qualities. Such an annotated CC can be used by a BS serving a UE to first localize the UE in the CC, and then to predict the signal quality from neighboring BSs. Each BS first constructs a CC from a number of samples, determining similarity of radio signals transmitted from different locations in the network based on covariance matrices. Then, the BS learns a continuous function for predicting the vector of neighboring BS SNRs as a function of a 2D coordinate in the chart. The considered algorithm provides information for handover decisions without UE assistance.

1.2. Collaborative Deep Learning

It has been firmly established that cooperation between wireless transmitters positively affects the network performance, leading to gains that would not be otherwise achievable. Given the fact that cooperative behaviours can be beneficial in a variety of domains ranging from e.g. resource (time/frequency/power) control to e.g. beam selection, they become the end goal of a multitude of networking problems.

Broadly speaking, cooperation entails the interaction of multiple entities finalized to pursue a common goal that is mutually beneficial. In wireless networks this definition encompasses all situations where transmitters need to design their communication parameters based on local observations of the channel state in order to maximize a common utility. A straightforward approach to establish cooperation relies upon a central processing unit gathering local observations from network devices and yielding the group decision as the output of an optimization program maximizing the metric of interest (or a surrogate of it). While being simple and yielding the best performance the centralized solution comes with many drawbacks, notably round trip delays and single point of failure vulnerabilities. These clash with the present network requirements put forward by Ultra Reliable and Low Latency (URLL) communications and they justify the growing interest for the decentralized counterpart of the coordination problem. In this setting, each device determines autonomously its action based only on local observations, possibly available with different precisions from device to device. As a result, the limits of coordination are posed by degree of correlation between CSI across devices and the true system state. It becomes of primary importance leveraging synthetic data generation procedures in order to investigate the limits of decentralized cooperation as a function of the properties of these probability distribution.

1.2.1. Role of Synthetic Data Generation in Collaborative Machine Learning

It is well-known that the ability of machine learning models to correctly predict labels of unseen data is positively affected by the size of the training dataset. However, obtaining large datasets by real world measurements and manual labeling can be costly and can arise privacy issues, for example when tracing sensible data like Global Positioning System (GPS) position, traffic packets, cached contents, etc. On the other hand, data generators allow

to mimic the behaviour of a real world phenomenon in a controlled fashion and provide tools to log quantities of interest, hence representing cheap and versatile alternatives in order to access large and possibly high fidelity datasets. The degree of control on the fabricated data and the active sampling capabilities offered by simulators allow to overcome many issues related to real-world measurements, such as unbalanced classes and under-represented events. For these reasons, in the context of wireless communications, where datasets are difficult to obtain by direct measurements but mature network simulators and precise mathematical models are available, synthetic data generation plays a key role.
Specifically for collaborative machine learning, synthetic data generation acquires even greater importance. The distributed information structure of multi-agent problems entails data logging at a network level across a multitude of different devices; moreover, both local observations and world state depend on the behaviour of agents, as a consequence datasets cannot be the result of a one-time sampling but they need to be generated in real-time during training in order to account for distribution shifts. These render real-world measurements even more cumbersome and potentially dangerous when the application at hand can harm humans or damage infrastructures (e.g. autonomous driving, robotics arms, etc.) Finally, the problem of model mismatch, that can hamper synthetic data generators to a point that the gains of accessing a larger dataset is nullified, becomes secondary in the context of multi-agent learning. In this setting dataset are used to study agent interactions and the effect of decentralized information structures on the coordination problems, rather than on investigating to what extent machine learning models can extract and exploit realistic patterns from simulated data. Therefore for collaborative machine learning the benefits of synthetic data surpass its drawbacks and explains why most of the research output in this field is based on fabricated datasets.

1.2.2. Data-Driven Solution of the Coordination Problem

With the purpose of highlighting the role of data-driven tools in the context of wireless coordination, we now formalize the decentralized coordination problem using team decision formalism.
A wireless coordination problem can be defined by the following quantities:

- K: the number of interacting wireless devices (decision makers).
- $\boldsymbol{s} \in \mathcal{S}$: the true state of the communication system.
- $\hat{\boldsymbol{s}}_j \in \hat{\mathcal{S}}_j$: the local information at device j about the system state.
- $\pi_j : \hat{\mathcal{S}}_j \to \mathcal{A}_j$: the strategy of user j, mapping local observations into communication parameters.
- $g : \mathcal{S} \times \prod_{j=1}^{K} \mathcal{A}_j \to \mathbb{R}$: a common network utility, function of the system state and the decision of the various wireless devices.
- $P_{s,\hat{s}_1,\ldots,\hat{s}_K}$: the joint distribution governing the relation between system state and the local observations at the wireless devices.

The solution to the coordination problem is a set of strategies that maximizes the expected utility and it is the result of the following functional optimization problem

$$(\pi_1^*, \dots, \pi_K^*) = \underset{\pi_1,\dots,\pi_K}{\arg\max}\, \mathbb{E}\left[g(\boldsymbol{s}, \pi_1(\hat{\boldsymbol{s}}_1), \dots, \pi_K(\hat{\boldsymbol{s}}_K))\right] \tag{1.1}$$

where the expectation is taken with respect to the random variables in bold.
The distributed nature of the information is one of the distinctive traits in decentralized coordination problems. Each decision maker j is endowed with a local observation $\hat{\boldsymbol{s}}_j$ that discloses only partial information about the world state $\boldsymbol{s}$ and other Decision Maker (DM) observation $\{\hat{\boldsymbol{s}}_i\}_{i\neq j}$. For instance, in a wireless network design problem $\boldsymbol{s}$ may represent the global channel state information matrix while $\hat{\boldsymbol{s}}_j$ can be a local feedback, noisy global feedback, hierarchical feedback, etc. Also note that the optimization variables in (1.1) lie in the space of functions. Functional optimization problems are notoriously difficult to tackle and in order to circumvent them it is customary to represent each policy π_i by a parametrized function $\pi_i^{\theta_i}$, recasting the original problem into the following

$$(\theta_1^*, \dots, \theta_K^*) = \underset{\theta_1,\dots,\theta_K}{\arg\max}\, \mathbb{E}\left[g(\boldsymbol{s}, \pi_1^{\theta_1}(\hat{\boldsymbol{s}}_1), \dots, \pi_K^{\theta_K}(\hat{\boldsymbol{s}}_K))\right] \tag{1.2}$$

A particular choice of parametrized policy is that offered by the output of a D (DNN) parametrized by θ_i. In this case the policies are realized by Team-DNNs that work cooperatively so as to solve the maximization problem in (1.2). This allows exploiting their approximation power and the efficient parameters optimization algorithms available (e.g. back-propagation), leading to a fully data-driven procedure to design decision policies. Namely, given that it is possible to sample a training set $\mathcal{D} = \{(s, \hat{s}_1, \dots, \hat{s}_K)_i\}_{i=1}^n \sim P_{s,\hat{s}_1,\dots,\hat{s}_K}^{\otimes n}$ [1] of size n, the neural networks can be trained using gradient ascent with the following empirical average of the objective function

$$\mathcal{U}(\theta_1, \dots, \theta_K) = \sum_{(s,\hat{s}_1,\dots,\hat{s}_K)\in\mathcal{D}} \frac{g(s, \pi_1^{\theta_1}(\hat{s}_1), \dots, \pi_K^{\theta_K}(\hat{s}_K))}{|\mathcal{D}|} \tag{1.3}$$

However, it is important to notice that the distributed information model abstains DMs from accessing the gradient information, which depends on the true state of the world and on the actions of the other DMs. As a result, the training phase has to be centralized with perfect information sharing, temporary violating the original decentralized information model and, only after convergence, the optimized models can be distributed to the different DMs for decentralized testing. This procedure goes under the name of “centralized training/decentralized testing" paradigm.

1.2.3. Distributed Power Control

Machine learning has proved to be extremely successful in extracting and leveraging patterns in real world data; nonetheless, synthetic data generation can be valuable, especially when the employed generative model well-represent the real world. In order to exemplify the generation of synthetic datasets we consider the distributed power control problem as a particular instance of the coordination problems in wireless networks.

[1] $P_{s,\hat{s}_1,\dots,\hat{s}_K}^{\otimes n}$ denotes the product measure $\underbrace{P_{s,\hat{s}_1,\dots,\hat{s}_K} \otimes \cdots \otimes P_{s,\hat{s}_1,\dots,\hat{s}_K}}_{n \text{ times}}$

The problem of distributed power control in interference channels with noisy CSIT can be formulated as a coordination problem in the sense (1.2), as seen below. Consider a K-user interference channel with single-antenna transmitters (Transmitter (TX)s) and receivers (Receiver (RX)s), in which TX i serves RX j with a maximum transmit power P_{max}. The decision makers are the K TX and the channel gain matrix $\boldsymbol{G} \in \mathbb{R}^{K \times K} \sim P_G$ is the system state. The local observation at TX i is $\hat{\boldsymbol{G}}_i$, a noisy estimate of channel gain matrix $\boldsymbol{G}$. In order to access a training set coming from the joint distribution $P_{G,\hat{G}_1,\ldots,\hat{G}_K}$ assumptions on the channel gain matrix distribution and the decentralized information models has to be done.
Assuming independent Rayleigh fading for each TX-RX pair, the channel gain matrix $\boldsymbol{G}$ can be obtained sampling each channel gain $G_{i,j}$ according to the Rayleigh distribution, namely

$$f(G_{i,j}) = \frac{2G_{i,j}}{\Omega_{i,j}} e^{-G_{i,j}^2/\Omega_{i,j}} \tag{1.4}$$

where $\Omega_{i,j}$ is the average power gain accounting for path loss and average blockage for the link between TX i to RX j.
A simple, yet versatile, model for the local channel information consists in assuming that the noisy estimate of the true channel gain matrix at user i obeys the following relation

$$\hat{\boldsymbol{G}}_i = \boldsymbol{\Gamma}_i \odot \boldsymbol{G} + \boldsymbol{\Gamma}'_i \odot \boldsymbol{\Delta}_i \tag{1.5}$$

where $\{\boldsymbol{\Gamma}'_i\}_{j,k} = \sqrt{1 - \{\boldsymbol{\Gamma}_i^2\}_{j,k}}$ with $\boldsymbol{\Delta}$ being a noise matrix (e.g. Independent and Identically Distributed (i.i.d). Rayleigh entries) and $\odot$ defines element wise product . The matrix $\boldsymbol{\Gamma}_i$ is linked to the CSI quality at user i. Each entry $\{\boldsymbol{\Gamma}_i\}_{j,k} \in [0, 1]$ represents the quality of channel gain information of the $j - k$ link and spans the range from the perfect channel gain information ($\{\boldsymbol{\Gamma}_i\}_{j,k} = 1$) to the case where local observation are completely uncorrelated with the true channel state ($\{\boldsymbol{\Gamma}_i\}_{j,k} = 0$).
Under these assumptions, synthetic datasets can be generated to train and to assess the performance of data-driven distributed power control policies. For instance, if the goal is to maximize the network sum-rate, under the assumption of Gaussian distributed with zero mean and unit variance information symbols and noise, the utility function can be expressed as

$$R(\boldsymbol{G}, P_1, \ldots, P_K) = \sum_{i=1}^{K} \log_2 \left(1 + \frac{G_{i,i}P_i}{1 + \sum_{j \neq i} G_{j,i}P_j}\right) \tag{1.6}$$

Parametric models, as DNNs, can then be used to implement the power control policies at the various transmitters

$$\pi_i^{\theta_i} : \hat{\boldsymbol{G}}_i \to P_i \in [0, P_{max}]. \tag{1.7}$$

Then, in order to tune the model a sampled dataset $\mathcal{D} = \{(\boldsymbol{G}, \hat{\boldsymbol{G}}_1, \ldots, \hat{\boldsymbol{G}}_K)_i\}_{i=1}^n \sim P^{\otimes n}_{\boldsymbol{G},\hat{\boldsymbol{G}}_1,\ldots,\hat{\boldsymbol{G}}_K}$ can be considered for maximizing the empirical utility function

$$\mathcal{U}(\theta_1, \ldots, \theta_K) = \sum_{(\boldsymbol{G},\hat{\boldsymbol{G}}_1,\ldots,\hat{\boldsymbol{G}}_K)\in\mathcal{D}} \frac{R(\boldsymbol{G}, \pi_1^{\theta_1}(\hat{\boldsymbol{G}}_1), \ldots, \pi_K^{\theta_K}(\hat{\boldsymbol{G}}_K))}{|\mathcal{D}|}. \tag{1.8}$$

1.3. Predictive Machine Learning for Multiuser Beamforming

mMIMO is a primordial technology for 5G wireless networks with main purpose to increase area spectral efficiency [6]. In massive MIMO, the base station is equipped with a very large number of antennas. Looking towards post-5G, researchers are defining a new generation of base stations that are equipped with an even larger number of antennas. The concept of LIS designates a large continuous electromagnetic surface able to transmit and receive radio waves. A key conceptual enabler that is recently gaining increasing popularity is Holographic MIMO (HMIMO) that refers to a low-cost transformative wireless planar structure comprised of sub-wavelength metallic or dielectric scattering particles, which is capable of shaping electromagnetic waves consistent with desired objectives [7]. These large surfaces are placed on walls for example and are easily integrable into the surroundings. In practice, LIS is composed of a collection of closely spaced tiny antenna elements. While the potential for communications of LIS is being investigated, sensing features must be taken into account. Indeed, such large surfaces contain many antennas that can be used as sensors of the environment based on the CSI. The main useful characteristic of CSI exploitation in LIS is its spatial consistency. That is, thanks to the disposition of the antenna elements compounding the surface, a really accurate and informative representation of the radio propagation environment can be acquired and, posteriorly, be treated as an image to meet the usage of computer vision algorithms.

One of the objectives of this project is to develop sensing techniques based on the CSI collected by the surfaces and provide a high resolution image of the propagation environment. The second objective is to exploit sensing to improve the design of wireless communications. The sensing techniques will be designed based on machine learning and computer vision techniques. For that we will use existing research in the fields of mMIMO systems and machine learning methods specially computer vision ones, in order to take advantage of the image information to construct feature maps making use of the CSI.

1.3.1. Holographic Sensing

A hologram is a recorded interference pattern as a result of constructive and destructive combinations of the superimposed light-wavefronts, i.e., a photographic recording of a light field [8]. In the wireless context, LIS could be described as a structure which uses electromagnetic signals impinging in a determined scatterer in order to obtain a profile of the environment. That is, we can use the received signal power received at each of the multiple elements of the LIS to obtain a high resolution image of the propagation environment. Using this approach, the complexity of the multipath propagation is reduced by representing it as an image. This provides a twofold benefit: *i)* the massive number of elements that composed the LIS leads to an accurate environment sensing, and *ii)* it allows the use of computer vision algorithms and image processing techniques to deal with the resulting image.

As an illustrative example, Fig. 1.2 shows the holographic images obtained for different propagation environments. Specifically, Figs. 1.2a and 1.2b correspond to a LoS propagation (no scatterers), whilst Figs. 1.2c and 1.2d were obtained from an industrial scenario with a rich scattering. Note that, in the case in which different scatterers are placed, their position and shapes are captured by the LIS and represented in the image. Thanks to the large aperture offered by the surface, we are able to reconstruct a feature map (image) that describes what is occurring in space, based on the information acquired from the radio propagation environment.

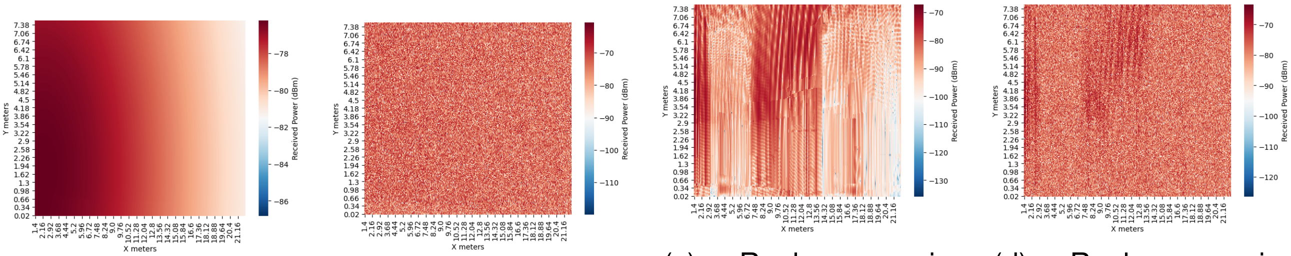

(a) LoS, noiseless. (b) LoS, noisy. (c) Real scenario, noiseless. (d) Real scenario, noisy.

Figure 1.2: An example of holographic measurements obtained via ray-tracing simulation.

1.3.2. LIS and Machine Learning for Sensing

Let us consider an industrial scenario where a robot is supposed to follow a fixed route, and assume that, due to arbitrary reasons, it might deviate from the predefined route and follow an alternative (undesired) trajectory. Hence, our goal is, based on the sensing signal transmitted by the target device, being able to detect whether the robot is following the correct route or not. In order to perform the anomalous route detection, let us assume that a LIS (i.e., a large array of closely spaced antennas), is placed in the scenario. Therefore, the sensing problem reduces to determine, from the received signal at each of the LIS elements, if the transmission has been made from a point at the desired route or from anomalous ones. Due to the fact that, in general, acquiring an accurate CSI is a non-trivial task, Let us resort on the received signal amplitude (equivalently, the received power), which may lead to a simpler system implementation. To understand the necessity of large arrays and ML techniques to tackle this problem, let consider the following preliminary example: Assume that we have two points, p_1 and p_2, belonging to the desired and the anomalous route, respectively. Then, the received complex signal vector at the array of M antennas from p_1 and p_2 is given by

$$\mathbf{y}_k = \mathbf{x}_k \mathbf{h}_k + \mathbf{n}_k, \quad k = 1, 2, \tag{1.9}$$

where $\mathbf{x}_k$ is the transmitted signal, $\mathbf{h}_k$ is the complex channel coefficients and $\mathbf{n}_k \sim \mathcal{CN}_M(\mathbf{0}, \sigma^2\mathbf{I})$ represents the noise vector. To verify that p_1 and p_2 are actually points belonging to different trajectories, we could try to perform an hypothesis testing based on the Euclidean distance between the received signal amplitudes, i.e.,

$$\frac{1}{M}|||\mathbf{y}_1| - |\mathbf{y}_2|||_2 \approx \frac{1}{M}\sum_{i=1}^{M} |y_{1,i}|^2 + |y_{2,i}|^2 - 2\mathrm{Re}\{|y_{1,i}||y_{2,i}|\}, \tag{1.10}$$

with $y_{k,i}$ denoting the elements of $\mathbf{y}_k$. If we consider that M is sufficiently large, then the law of large numbers holds and (1.10) is rewritten as

$$\frac{1}{M}\||\mathbf{y}_1| - |\mathbf{y}_2|\|_2 = \frac{1}{M}\sum_{i=1}^{M}\left[|h_{1,i}|^2 + |h_{2,i}|^2\right] + 2\sigma^2 - \frac{2}{M^2}\sum_{i=1}^{M}|y_{1,i}|\sum_{i=1}^{M}|y_{2,i}|. \tag{1.11}$$

In (1.11), the first term is the sum of the average power of the channels, whilst the second term represents the equivalent noise, which completely depends on the channel realizations. If we would perform an hypothesis testing in order to establish a certain threshold that determines if the two points are in different routes, then the variance of the error term would determine the probability of failure. Note that, to obtain an optimum estimator, we would need to know all the possible states of the channels for each path. Moreover, even in the most simple case, i.e., assuming a pure LoS propagation, we would still be unable to distinguish if the two points are in different trajectories or at distinct positions of the same route.

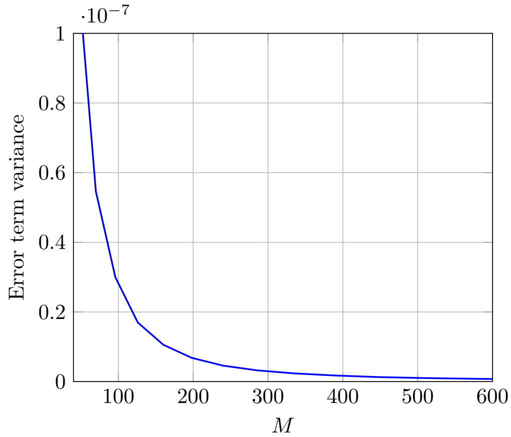

Figure 1.3: Equivalent noise term variance in terms of M in a LoS scenario for $\sigma^2 = 10^{-6}$.

The use of a very large number of antennas arises as a possible solution to mitigate the effect of the noise term. For the sake of illustration, Fig. 1.3 depicts the variance of the noise term as a function of the number of antenna elements in a pure LoS propagation environment, showing clearly how the variance tends to zero as the number of antennas increases.

However, although the use of a large number of elements in the LIS may reduce the noise variance, in a realistic environment, the complexity of the propagation paths is considerable, and the theoretical analysis becomes cumbersome and site-dependent. Hence, in order to gain insight into how the propagation paths between different positions translate into differences in the received signals, we have to resort on machine learning algorithms. This, together with the use of LIS, can provide the necessary information about the propagation environment in order to perform the anomalous route detection.

1.3.3. Channel Model for LIS

In order to validate the proposed method, we can carry out an extensive set of simulations to analyze the performance of the classification algorithm based on holographic images. To properly obtain the received power values, we make use of a ray-tracing model, so we can capture the effects of the multipath propagation in the most reliable way. Ray-tracing is a strategy which leads to provide very accurate results [9, 10], although its computational cost increases exponentially with the maximum allowed number of paths [11].

1.3.4. Received Power and Noise Modeling

The complex electric field $\widetilde{E}_i(t)$, arriving at the i-th antenna element at sample time t, can be regarded as the superposition of each path, i.e.,

$$\widetilde{E}_i(t) = \sum_{n=1}^{N_r} \widetilde{E}_{i,n}(t) = \sum_{n=1}^{N_r} E_{i,n}(t) e^{j\phi_{i,n}(t)}, \tag{1.12}$$

where N_r is the number of paths and $\widetilde{E}_{i,n}(t)$ is the complex electric field at i-th antenna from n-th path, with amplitude $E_{i,n}(t)$ and phase $\phi_{i,n}(t)$. From (1.12), and assuming isotropic antennas, the complex signal at the output of the i-th element is therefore given by

$$\widetilde{V}_i(t) = \sqrt{\frac{\lambda^2 Z_i}{4\pi Z_0}} \widetilde{E}_i(t) + n_i(t), \tag{1.13}$$

with $\lambda = 8.5cm$ wavelength, $Z_0 = 120\pi$ the free space impedance, Z_i the antenna impedance, and $n_i(t)$ is complex Gaussian noise with zero mean and variance σ^2. For simplicity, we consider $Z_i = 1 \, \forall \, i$. Thus, the power $W_i(t) = |\widetilde{V}_i|^2$ is used at each temporal instant t to generate the holographic image. Finally, in order to test the system performance under distinct noise conditions, the average SNR, γ, is defined as

$$\gamma \triangleq \frac{\lambda^2}{4\pi Z_0 M T \sigma^2} \sum_{t=1}^{T} \sum_{i=1}^{M} |\widetilde{E}_i(t)|^2, \tag{1.14}$$

where T the number of time steps (positions of the robot) simulated in the ray-tracing software[2].

[2] For more details, please refer to [12]

2. Radio Channel Characteristics & Modeling

As compared to 4G standards, 5G is envisioned for network densification using smaller cell zones and capacity enhancement by exploiting mMIMO antenna arrays at BSs and smaller arrays at the mobile UE. mm-Wave spectrum (from 30 GHz to 300 GHz) is a key ingredient for 5G and B5G wireless systems due to its tremendous amount of raw available bandwidth. However, an accurate understanding of the performance of radio signals when they propagate through a radio channel is needed. Therefore modeling of the radio channel is vital to wireless communications research [13].

2.1. Propagation Principles

Channel models characterize wireless channels and used to analyze performance of system in a given scenario. A proper channel model should be able to reproduce the channel parameters obtained via real-world measurements and provide an acceptable performance prediction. Since 5G wireless systems are expected to utilize mm-Wave frequency bands, modeling of mm-Wave channels are in huge need and important. A radio channel is defined as a medium linking a TX to a RX terminal. Due to presence of various objects in the surrounding environment radio waves may experience reflection, scattering or diffraction, arriving at the RX with different paths and delays. Thus, the received signal is the sum of multiple radio waves with different phases and delays. As defined in the 3rd Generation Partnership Project (3GPP) channel model [14] the transmitted signal is decomposed into several time and space clusters.
Signal variation is classified as LSF and Small-Scale Fading (SSF) [15]. LSF is considered as the average channel gain over a long distance (tens to a few hundred wavelength), and is caused by large terrestrial obstructions between TX and RX. SSF is considered as variation of signal over a short distance (fractions of wavelength). The standard deviation in propagation time between MPC is the Root Mean Square (RMS) delay, and the standard deviation of angels between MPCs is the RMS angular spread.

2.1.1. Path Loss and Large-Scale Fading Model

A starting point for evaluation of large-scale parameters of wireless channel is the free space propagation of radio waves. Path loss is the attenuation of radio wave energy as it propagates through the channel and is defined as [16]

$$PL[dB] = 10\log_{10}\frac{P_T}{P_R} \tag{2.1}$$

where P_T and P_R are transmitted and received power, respectively. The received power in free space depends on propagation distance d and operating wavelength of transmission λ and is defined as [16]

$$P_R = P_T G_T G_R \left(\frac{\lambda}{4\pi d}\right)^2 \tag{2.2}$$

where G_T and G_R are the antenna gains at the TX and RX, respectively [9]. By comparing the free space path loss at MHz frequencies up to several GHz, one can simply show

that moving up to mm-Wave frequencies we must compensate for 20-40 dB received power loss when compared with current microwave bands. The path loss increment at mm-Wave bands has been confirmed by several measurement campaigns [17, 18]. However, this is not the whole story. There is a hidden benefit of propagating at mm-Wave frequencies which is substantial gain of small directional antennas. In particular, by using array antennas and steerable narrow beams, energy can be concentrated in favorable directions which can decrease path loss dramatically. Other sources of path loss in mm-Wave frequencies are atmospheric attenuation of Oxygen and rain attenuation that contribute to reduction of received signal power but it does not become significant until carrier frequencies exceed 50 GHz. In real environment, there are more obstacles and path loss is more severe than free space, thus field measurement and path loss modeling is needed. For mm-Wave, several field measurement have been carried out [19, 20].
Shadowing is more significant in higher frequencies due to higher diffraction losses. Shadow fading has various sources one of which is by environmental objects such as walls, cars, human, and vegetation that block a MPC, hence path is attenuated. The other form of shadow fading is caused by UE movement, as it moves along a trajectory and passes by coverage region of the BS power variations occur. Even the orientation of UE and change of hold can cause shadowing.

2.1.2. Small-Scale Fading

Small-scale fading is rapid fluctuation of radio signal amplitude over a short distance or time interval. It is due to the receiving of two or more versions of the transmitted signal with different delays. Factors such as multi-path propagation, velocity of UE, moving surrounding objects, and transmission bandwidth of the signal influence small-scale fading. In fact, it is incorporated in Channel Impulse Response (CIR). The CIR of a narrowband flat fading channel can be written as [16]

$$h(t, \tau) = C + g(t, \tau) \tag{2.3}$$

where C is a complex and deterministic component, corresponding to Line-of-Sight (LOS) link, and $g(t, \tau)$ is typically a complex zero mean Gaussian random variable whose envelope has a Rayleigh distribution and τ corresponds to the excess delay. Nonetheless, if LOS component is available, the amplitude will have the Ricean distribution. By increasing the channel bandwidth, due to delays of paths, RX can have more resolvable path, thereby the CIR will change to a Tapped Delay Line (TDL) model. At mm-Wave frequencies, objects that counting as scattering objects at microwave frequencies will become reflectors due to the fact that reflections mostly occurs on objects that are comparably much larger than the operating wavelength, thus multipath delay spread could be significantly affected by the structure and composition of the environment [17]. Small scale fading was not considered correlated in majority of literature on mMIMO, which in turn hinder reliable investigation of millimeter-Wave (mm-Wave) mMIMO channel. Recently, it has gained a lot of attention in wireless community [21] and effect of that has been investigated.
Doppler effect at mm-Wave bands is magnified due to higher frequencies. However, it is expected that by utilizing directional antennas and wider bandwidth, this effect can be overcome. Highly directional antennas can reduce frequency selectivity generated by interference between MPCs. Orthogonal Frequency Division Mutiplixing (OFDM) in wideband systems inherently experience more frequency selectivity. This problem can be mitigated with

highly directive antennas [9].

2.2. System Modeling

Measurement results are turned into channel models through different methods and they could be classified into different categories; one classification method is to divide models into analytical and physical [22]. The analytical models do not explicitly take the wave propagation properties into consideration. Channel coefficients with a specific statistical distribution characterize the wave propagation in a scattering environment. The Kronecker channel model is an example of analytical model. On the other hand, physical models characterize the channel based on the fundamental laws of electromagnetic wave propagation. Wave propagation parameters such as complex amplitude and MPC delay are explicitly modeled. 3GPP channel model is an example of physical models. Authors in [23] provide a detailed review of some existing MIMO channel models. In this study channel models are categorized in three distinct groups, namely, deterministic model, stochastic models, and hybrid models. We divide the channel models to analytical and physical and then subdivide each one to different categories.

2.2.1. Modeling Principles

Physical MIMO channel models can be subdivided into three distinct categories: *deterministic models*, *geometrically based stochastic models*, and *non-geometrical stochastic models* The first category is the **deterministic** or measurement based models. Channel models are designed based on field measurements. Ray-tracing is a well known model which uses geometrical and electrical properties of environment and information of antennas such as radiation pattern, polarization, and carrier frequency to determine the channel impulse response. To be more specific, the channel simulator models the path loss experienced by the multi-path components using the free-space path loss model with power inversely proportional to the square of the distance. The reflections from obstacles, i.e., the walls, are modeled such that the reflection coefficients are based on Fresnel's equations. The channel for each link is then calculated using the ray-traced paths with the path loss, reflection losses, and antenna gain accounted for in the channel [5]. This modeling approach is very accurate compared to other models, however, high computational time and cost, calibration difficulty are its drawbacks.
The second category is the **geometrically based stochastic models**. In order to be more realistic, the electromagnetic wave propagation laws and geometry of the propagation environment is applied to these models. Parameters such as AoA of the transmitted signal, Azimuth angle-of-Departure (AoD) of received signal, and the azimuth spread characterize the channel model. Moreover, the effect of objects on the propagation channel is modeled by scatterer distributions. The stochastic distribution of scatterers aids the model to be more realistic.
The one-ring model is a used for macro-cellular networks and lies within stochastic geometrically based models [24]. The TX is assumed to be above all scatterers and the RX is surrounded by local scatterers. Based on the environment, various scatterer distributions are considered and signals aggregate at the RX from different directions. No LoS path is considered between the TX and the RX, and single bounce scattering with equal power of

scattered rays is considered. From the model, correlation matrices between antenna elements could be obtained, nonetheless, it cannot completely describe all observed channel effects of MIMO channel.
The Quasi Deterministic (QD) model is a combination of deterministic and stochastic models. To be more precise, given an environment and TX and RX positions, a basis for channel-Deterministic rays (D-rays)- could be computed through ray-tracing. In fact, D-rays are the strongest propagation paths. The delivered signal power over each of the rays is calculated by considering theoretical formulas. Then, based on these rays, MPCs are randomly generated by the QD model. The generation of a channel based on QD model has been elaborated in [25] and results are validated with measurement data.
The third category is the **non-geometrical stochastic models**. This model determines the MIMO channel parameters (AoD, AoA, delay, etc.) in a completely stochastic manner by assigning a probability distribution function to each parameter and does not take into account the geometry of the environment. The extended Saleh-Valenzuela model has been proposed in [26]. The model is based on the assumption that angular parameters (AoA, AoD) statistics are identical and independent which allow the spatial clusters to be characterized in terms of their mean cluster angle and angular spread. Also, the mean delay of each cluster is modeled by a Poisson process.
Analytical models can be split into *propagation based models* and *correlation based models*. The **propagation based models** describe the channel matrix via propagation parameters. The maximum entropy model [27] and the finite scatter models [28] belong to this category. The **correlation based models** describe the MIMO channel model in a stochastic manner and in terms of correlation between the channel matrix entries. The Kronecker [29] and Weichselberger [30] models are examples of this category. In this category one of the simplest models which is widely used in the literature is the Independent and i.i.d MIMO channel. It assumes a random channel matrix with zero mean and i.i.d elements. Since it assumes transmission is occurred in a rich scattering area with enough antenna spacing, the channel fade is statically independent. Whereas, in reality the environment has less scatterers and the small spacing implies correlation between channel matrix entries. Therefore, the i.i.d model is used in general for mathematical analysis and to give an upper bound of the performance.
The Kronecker model was used for capacity analysis initially. It assumes that spatial correlation at TX and RX is independent which is equivalent to restricting the channel model to a rich scattering environment. Also, the channel covariance matrix is defined as Kronecker product of covariance matrix at each end of the links. The drawback of Kronecker model is that it overlooks the interdependence of both ends of the MIMO channel; in other words it is not able to address the couplings between transmit and receive side of the MIMO channel. Measurements showed that mm-Wave MIMO channel is a non-Kronecker, the deviation from Kronecker model was estimated for several scenarios [30].

2.2.2. Channel Models

We consider a mMIMO mm-Wave cellular system where the BS has M antenna elements and each UE has N antenna elements. For simplicity, we assume that the BS and UEs are equipped with horizontal Uniform Linear Array (ULA), with an extension to other array geometries is straight forward. The scattering environment is depicted in Figure 2.1. The narrowband time varying channel gain (time development) between the BS and the UE can be represented in terms of MPCs as [31]:

$$\boldsymbol{H}(t) = \frac{1}{\sqrt{L}} \sum_{k=1}^{K} \sum_{l=1}^{L} g_{k,l}(t)\ \boldsymbol{a}_{BS}(\theta_{k,l})\ \boldsymbol{a}_{UE}^{H}(\phi_{k,l}). \tag{2.4}$$

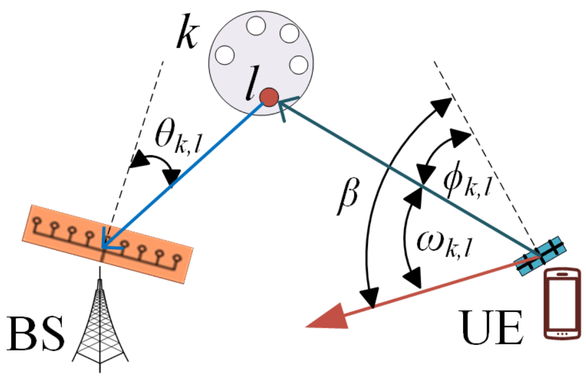

Figure 2.1: Scattering environment.

There are K clusters, and in each cluster there are L MPCs. The complex small-scale fading coefficient on the lth sub-path of the kth cluster is $g_{k,l}(t)$, and $\boldsymbol{a}_{BS} \in \mathbb{C}^{M\times 1}$ and $\boldsymbol{a}_{UE} \in \mathbb{C}^{N\times 1}$ are the vector responses for the BS and UE antenna arrays. The AoA and AoD are $\theta_{k,l}$ and $\phi_{k,l}$. For each cluster there is a cluster angular spread of arrival $\sigma_{k,\mathrm{BS}}$ and departure $\sigma_{k,\mathrm{UE}}$, such that $|\theta_{k,l} - \theta_{k,l'}| \leq \sigma_{k,\mathrm{BS}}$ and $|\phi_{k,l} - \phi_{k,l'}| \leq \sigma_{k,\mathrm{UE}}$. For ULA, the response vector is

$$\boldsymbol{a}(\theta) = [1, e^{j\frac{2\pi}{\lambda} s \sin(\theta)}, \dots, e^{j\frac{2\pi}{\lambda}(N_r-1)s\sin(\theta)}]^T, \tag{2.5}$$

where λ is the carrier wavelength, s is the antenna spacing and N_r the number of antenna elements. The UE moves in a direction β relative to the orientation of its antenna array. The small scale fading coefficient can then be modeled as [31]:

$$g_{k,l}(t) = \bar{g}_{k,l}\ e^{2\pi j t f_D \cos(\omega_{k,l})},\ \bar{g}_{k,l} \sim CN(0, \gamma_k 10^{-\alpha/10}), \tag{2.6}$$

where f_D is the maximum Doppler shift, $\omega_{k,l} = \beta - \phi_{k,l}$ is the angle of arrival of the subpath relative to the direction of motion, α is the omnidirectional path loss and γ_k is the fraction of power in the cluster. The relation between $\omega_{k,l}$ and the angle of arrival depends on the orientation of the mobile terminal relative to motion.
The channel model between the BS and the UE for a given subcarrier n can also be represented as [32] by taking into account the elevation angles:

$$\boldsymbol{H}(n) = \frac{1}{\sqrt{L\sum_l K_l}} \sum_{l=1}^{L} \sum_{k=1}^{K_l} g_{k,l} e^{-2\pi b \tau_{k,l}/T}\ \boldsymbol{a}_r(\theta_{k,l}, \varphi_{k,l})\ \boldsymbol{a}_t^H(\phi_{k,l}, \psi_{k,l}). \tag{2.7}$$

There are K clusters, and in each cluster there are L MPCs. Superscripts r and t denote receiver and transmitter respectively, $\boldsymbol{a}_r \in \mathbb{C}^{M\times 1}$ and $\boldsymbol{a}_t \in \mathbb{C}^{N\times 1}$ are the vector responses for the receiver and transmitter antenna arrays. The path loss on the lth sub-path of the kth cluster is $g_{k,l}$ and the corresponding propagation delay is $\tau_{k,l}$. T is the OFDM symbol duration. The AoA and EoA at the receiver are $\theta_{k,l}$ and $\varphi_{k,l}$. The AoD and Elevation angle-of-Departure (EoD) at the transmitter are $\phi_{k,l}$ and $\psi_{k,l}$. Similarly, for all angular parameters in each cluster, angular spread is defined such that $|\theta_{k,l} - \theta_{k,l'}| \leq \sigma_{k,\text{BS}}$, $|\varphi_{k,l} - \varphi_{k,l'}| \leq \delta_{k,\text{BS}}$, $|\phi_{k,l} - \phi_{k,l'}| \leq \sigma_{k,\text{UE}}$, and $|\psi_{k,l} - \psi_{k,l'}| \leq \delta_{k,\text{UE}}$. The channel matrix of UE i at the BS using subcarrier n is denoted as

$$\mathbf{H}_i(n) \in \mathbb{C}^{M \times N} \tag{2.8}$$

Where M is number of antenna at BS and N is number of antenna at UE. In order to describe the spatial behavior of the two ends of a MIMO channel, a full correlation matrix that specifies the $MN \times MN$ mutual correlation values between all channel matrix elements is required, given as $\boldsymbol{R} = \mathbb{E}_{\boldsymbol{H}}\{\text{vec}(\boldsymbol{H})\text{vec}(\boldsymbol{H})^H\}$. A drawback of the full covariance matrix is that it requires significant pilot transmissions to be estimated. In addition, direct interpretation of the elements of $\boldsymbol{R}$ with respect to the physical propagation of the channel is difficult.
The raw instantaneous covariance matrix of UE i at the BS without considering UE's beamformer (but with beamformer at the other end) is defined as

$$\mathbf{R}_i = \frac{\sum_n \mathbf{H}_i(n)\mathbf{H}_i^H(n)}{B} \tag{2.9}$$

where B is the number of subcarriers. It should be noted that this representation of covariance matrix only applies to the Kronecker channel model.
A mm-Wave stochastic MPC channel model, gives rise to a non-Kronecker correlation structure, because the two ends of the channel cannot be considered independent. Hence, the one-sided correlation matrices are affected both by the statistical signal properties and the transmission covariance applied at the other link end.
The BS-side channel covariance matrix is defined as

$$\boldsymbol{R}_{BS} = \boldsymbol{R}_{BS}(\boldsymbol{Q}_{UE}) \equiv \mathbb{E}_{\boldsymbol{H}}\{\boldsymbol{H}\boldsymbol{Q}_{UE}\boldsymbol{H}^H\} \tag{2.10}$$

while the UE side covariance is

$$\boldsymbol{R}_{UE} = \boldsymbol{R}_{UE}(\boldsymbol{Q}_{BS}) \equiv \mathbb{E}_{\boldsymbol{H}}\{\boldsymbol{H}^H\boldsymbol{Q}_{BS}\boldsymbol{H}\}\ . \tag{2.11}$$

The covariance matrix at one end of a link depends on the transmission covariance at the other end. The matrices $\boldsymbol{Q}_{BS}$ and $\boldsymbol{Q}_{UE}$ represent the spatial signal covariance matrices at the BS-side and UE-side, respectively. For Kronecker channel models, the full channel covariance is a tensor product $\boldsymbol{R} = \boldsymbol{R}_{BS}(\boldsymbol{I}_N) \otimes \boldsymbol{R}_{UE}(\boldsymbol{I}_M)$, where $\boldsymbol{I}_P$ is the identity matrix of size P. This further implies that the angular spectrum at the BS, i.e. the eigenvectors of $\boldsymbol{R}_{BS}$, and the relative values of the eigenvalues, does not change when $\boldsymbol{Q}_{UE}$ is modified, and vice versa. The only dependence of BS covariance on $\boldsymbol{Q}_{UE}$ is that the total received power changes, the eigenstructure is otherwise the same [30].
The mm-Wave MPCs-channel model is a *non-Kronecker* model. A general channel matrix (One sample of the channel matrix is considered, i.e., the time development is not considered in this model.) can be modeled following Weichselberger & et. al. [30] as:

$$\boldsymbol{H} = \boldsymbol{U}_{BS}(\tilde{\boldsymbol{\Lambda}} \odot \tilde{\boldsymbol{H}})\boldsymbol{U}_{UE}^H, \tag{2.12}$$

where $\odot$ is the element-wise product of two matrices, $\tilde{\boldsymbol{H}}$ is a random matrix with i.i.d. zero-mean complex entries with unit variance, $\tilde{\boldsymbol{\Lambda}}$ is the element-wise square root of the coupling matrix given by $[\boldsymbol{\Lambda}]_{m,n} = \mathbb{E}_{\boldsymbol{H}}\{|\boldsymbol{u}_{BS,m}^{H}\boldsymbol{H}\boldsymbol{u}_{BS,n}|^2\}$. The coupling matrix specifies the average amount of energy that is coupled from the mth Eigenvector of the BS side to the nth Eigenvector of the UE side, $\boldsymbol{U}_{BS} = [\boldsymbol{u}_{BS,1}, \dots, \boldsymbol{u}_{BS,M}]$ and $\boldsymbol{U}_{UE} = [\boldsymbol{u}_{UE,1}, \dots, \boldsymbol{u}_{UE,N}]$ are the BS-side and UE-side spatial Eigenbases.

2.2.3. Base Station Deployment Models and Cell Layouts

Due to usage of high frequencies in mm-Wave bands, 5G New Radio (NR) deployments require dense network topologies which results in small-cell deployment scenarios. Each scenario has focused on specific properties and requirements related to the physical limits of mm-Wave communication and possible use cases. Urban Macro (UMa) is deployed for large coverage, and Urban Micro (UMi) is integrated with UMa to form heterogeneous networks [33]. For large areas, a huge number of mm-Wave small cells provide almost full coverage, however, high cooperation among small-cells and beamforming is required. UMi covers large indoor areas (also multiple open spaces and rooms is covered), because the UMa is unable to provide an in-depth coverage for indoor users.

As an example, for dense urban scenarios two options are adopted with one sector deployment for micro cells [34]. First option is that each BS antenna element has an omnidirectional pattern in horizontal domain and a directional antenna element (with 5dBi gain and Half Power Beam Width (HPBW)=40°) in vertical domain. Second option is that to use directional antenna elements in horizontal and vertical domain (with 8dBi gain HPBW=65°). The simplified radiation pattern of a single antenna element in horizontal space is depicted in Figure 2.2.

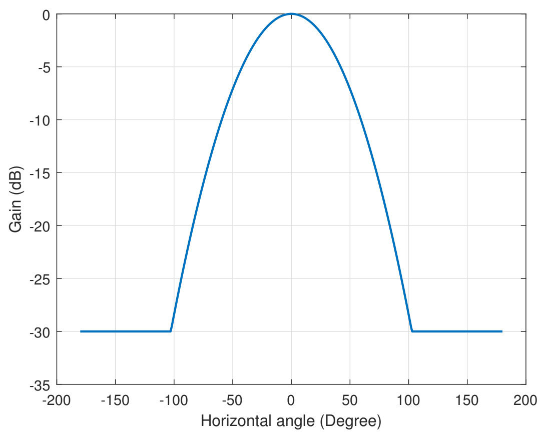

Figure 2.2: Simplified radiation pattern of a single antenna element.

2.2.4. Antenna Arrays and Architectures

Thanks to short wavelength of mm-Wave frequencies, using large scale antenna arrays is possible. ULA antenna is the simplest form of array antenna and is an ensemble of N antenna elements spacing equally on a straight line. The most common element is a dipole antenna. Array antennas are used to address the SNR improvement problem and response (gain) enhancement in particular directions. Thus, by using steerable beams in ULAs the array can accept signals from a particular direction and reject signals from other directions.

Consider and example of a ULA (with element spacing distance of s/λ) and a single propagation path. Let θ be the angle of incidence for the signal with respect to the boresight direction (AoA for the RX and AoD for the TX). The array response for a ULA is defined as (2.5). If we assume a single propagation path between TX and RX, with the complex gain of α, the channel would be $\boldsymbol{H} = \alpha\mathbf{a}(\theta_{\mathbf{r}})\mathbf{a}(\phi_{\mathbf{t}})^{\mathbf{H}}$. Since there is only one path, the channel rank is one and the channel is sparse. Using definition of narrow-band MIMO system with beamforming as:

$$y[n] = \mathbf{w}\boldsymbol{H}\mathbf{fs}[\mathbf{n}] + \mathbf{wv}[\mathbf{n}] \tag{2.13}$$

Where, $y[n]$ is the vector of sampled observation, $\mathbf{w}$ is the receive beamforming (combining) vector, $\mathbf{f}$ is the transmitting beamformer, $s[n]$ is the symbol stream and $\mathbf{v}$ is the noise vector. The optimum beamformer for this channel is $\mathbf{f} = \frac{\mathbf{1}}{\mathbf{N_t}}\mathbf{a}(\phi_{\mathbf{t}})$ where the combining vector is $\mathbf{w} = \mathbf{a}(\theta_{\mathbf{r}})$. Thus, the entries are just phase shifts and in case of analog beamformers, with a an optimization problem the best phase shift for each antenna will be chosen. Transmit and receive beamformers design is an important research area and has been studied in [35].
Based on 3GPP standards [14], for BS antenna Uniform Planer Array (UPA) is chosen. Antenna comprises of panels which are spaced with a specific distance in the horizontal and vertical directions. Antenna elements in each panel are spaced in horizontal and vertical directions with a specific spacing as well. Antenna panels are either single or dual polarized. The antenna radiation pattern of each antenna element is generated according to Table 2.1 [14, Tab. 4]. Horizontal cut of the radiation power pattern is shown in Figure 2.2, as well. $A''_{dB}(\theta'', \phi'')$ is the 3D antenna radiation power pattern as a function of azimuth angle θ'' and elevation angle ϕ''. A_{max} is the maximum attenuation power, SLA_V is the side-lobe attenuation in vertical direction, and θ_{3dB} and ϕ_{3dB} are vertical and horizontal 3 dB beamwidth of an antenna, respectively. Spatial multiplexing is one of the array antenna benefits and concisely it allows transmission of multiple symbols using the same radio resources (i.e. at the same time on the same carrier, with the same total power) as if only one symbol were transmitted [36]. It should be noted that selecting an array structure is a challenging problem, since some areas may need narrow beams in the azimuth and some may need narrow beams in the elevation.

Parameter	**Value**
Vertical cut of the radiation power pattern (dB)	$A''_{dB}(\theta'', \phi'' = 0°) = -min\left\{12\left(\frac{\theta''-90°}{\theta_{3dB}}\right)^2, SLA_V\right\}$ with $\theta_{3dB} = 65°$, $SLA_V = 30dB$ and $\theta'' \in [0°, 180°]$
Horizontal cut of the radiation power pattern (dB)	$A''_{dB}(\theta'' = 90°, \phi'') = -min\left\{12\left(\frac{\phi''}{\phi_{3dB}}\right)^2, A_{max}\right\}$ with $\phi_{3dB} = 65°$, $A_{max} = 30dB$ and $\phi'' \in [-180°, 180°]$
3D radiation power pattern (dB)	$A''_{dB}(\theta'', \phi'') = -min\{-(A''_{dB}(\theta'', \phi'' = 0°) + A''_{dB}(\theta'' = 90°, \phi'')), A_{max}\}$
Maximum directional gain of an antenna element	8 dBi

Table 2.1: Radiation power pattern of a single antenna element

In [37], Uniform Circular Array (UCA) is proposed for BSs. It claims higher directivity and array gain compared to other array architectures, as circular antenna array occupies a larger area with the same number of antenna elements. The other advantage of exploiting circular arrays for outdoor deployments is the 2π coverage area due to axial symmetry. This results in non-fluctuating gain of antenna's main lobe pattern. Thus, the antenna array is not affected by the angle variations caused by moving objects or array vibration.

2.3. mm-Wave and Microwave Propagation Differences

Radio waves have different characteristics at different frequency bands, thus we can anticipate different channel behavior at mm-Wave bands as compared to sub 6 GHz bands. The main differences are high path loss, penetration and reflection properties of common materials at high frequencies. For instance, due to comparable dimension of operating wavelength and foliage, scattering of the leaves increases whereas penetration through them decreases. In this section key differences of mm-Wave and microwave bands are explained.

2.3.1. Attenuation and Blockage

Increased path loss in mm-Waves is not only due to high frequencies, but also weather condition has impact on attenuation due to dimension order of rain droplets, hail stones and snowflakes and mm-Wave wavelength. mm-Wave systems are more sensitive to blockage by objects than microwaves. In [38], the authors have studied penetration loss and reflectivity at 28 GHz of different materials. Measurements show high reflectivity and penetration loss of outdoor building material and bricks in pillar. For instance, tinted glass had a penetration loss of 40.1 dB loss whereas, a clear non-tinted glass showed a 3.9 dB penetration loss. Thus, for indoor-to-outdoor penetration loss there is a distinct difference from microwave systems, however, indoor-to-indoor or outdoor-to-outdoor attenuation is less severe due to outdoor reflectivity and low attenuation of indoor materials.

2.3.2. Channel Sparsity

It is commonly believed that mm-Wave channels are sparse in angular and delay domain which means the number of dominant paths is limited. Based on the existing measurements in mm-Wave bands majority of angular or delay bins do not include MPCs with significant energy in contrast to microwave bands [39]. Due to sparse structure of MPCs, compressed sensing methods are able to effectively estimate the CSI with few measurements and reduced complexity [35].

2.3.3. Large Bandwidth and Large Antenna Arrays

Multi Gigabit-per-second (Gbps) data rates to UE have been offered by 5G NR that will use mm-Wave frequencies. Studies show that a 1 GHz wide channel at 28 GHz could offer several Gbps of data rate at the UE [40]. Also, there are large portion of raw spectrum at mm-Wave bands. Small wavelengths make it feasible to use large array of antennas in form of ULA and UPA. The authors in [41], has proposed use of lens antenna arrays and compared its performance to UPAs. Numerical results showed a significant reduction of signal processing complexity and Radio Frequency (RF) chain cost with no performance degradation.

2.3.4. Spatial Consistency and Stationary Regions

Spatial consistency represents the smooth variations for the stationary channels when a user moves or when multiple users are located in area over 5-10 m [42]. In other words, channel characteristics for closely located UEs are highly correlated. Spatial consistency covers a range of aspects such as small and large scale parameters, AoAs, and AoDs. Thus, 5G systems require a channel modeling whose parameters continuously evolve. One use case of spatial consistency could be beam tracking approaches when a UE moves along a trajectory. In [43] estimation of large-scale parameters from UE-specific channel covariance matrices measured at BSs and their spatial consistency in mm-Wave environment are investigated.
The small-scale spatial auto correlation coefficient of the received signal amplitude decreases rapidly over distance, and the correlation of individual MPC amplitude in a wideband (1 GHz) transmission is only 1-33 wavelengths depending on antenna pointing angle with respect to a scattering object, e.g. at 73 GHz, the correlation distance is less than 15 cm. The large-scale parameters have a much longer correlational distance of 12-15 m, since the scattering environment does not change dramatically in a local area [13]. Another important part of channel modeling is channel stationarity. Measurements have indicated that spatial stationary regions at microwave bands are much larger than mm-Wave bands [44]. It should be noted that orientation of directional antennas can impact correlation distances. Also, there has observed a sharp drop in received power in corners where a UE transitioned from LOS region to Non Line of Sight (NLoS). Therefore, stationary regions should carefully took into consideration for mm-Wave channel modeling.
In order to investigate spatial consistency of mm-Wave channel model based on the covariance matrix some of similarity measures need to be explained.

1. *Chordal distance*: The chordal distance is a widely used distance metric between subspaces. Given the covariance matrices of two UEs (locations) i and j, at the BS the chordal distance is defined as:

$$d_{Chord}(i,j) = \|\mathbf{R}_i^2 - \mathbf{R}_j^2\|_F \tag{2.14}$$

   Looking into the definition, we expect that the chordal distance shrinks when two users' distance decreases. Actually, if the chordal distance between two users is less than a predefined threshold, they are considered spatially correlated [42].

2. *CMD*: The similarity measure based on CMD is a normalized value and is defined between covariance matrices of two UEs (locations) i and j as:

$$d_{CMD}(i,j) = 1 - \frac{|Tr(\mathbf{R_i R_j})|}{\|\mathbf{R_i}\|_F \|\mathbf{R_j}\|_F} \tag{2.15}$$

   $d_{CMD} = 1$ in the case of orthogonal covariance matrices, and $d_{CMD} = 0$ when covariance matrices are collinear. Thus, for small values of d_{CMD} UEs are considered spatially correlated.

3. *Euclidean distance*: The Euclidean distance between two UEs (locations) i and j is simply defined as:

$$d_{Euc}(i,j) = \|\mathbf{R}_i - \mathbf{R}_j\|_F \tag{2.16}$$

As already mentioned, mm-Wave stochastic model gives rise to non-Kronecker correlation structure and subsequently, leads to two kinds of problem related to spatial consistency: First, the covariance matrix measured by a BS from uplink transmissions depends on the UE beamformer used for transmission. Second, the covariance measured by the BS depends on the direction of movement of the UE. We show that these problems can be mitigated by applying coordinated uplink precoding, such that geometrically consistent radio features can be extracted from covariance matrices estimated at the BS.

2.3.5. Multi-path Components and their Clustering

A major difference of mm-Wave to microwave frequencies is the small number of MPCs. The most of mm-Wave campaigns are inherently non-coherent since the narrow beamwidth of directional antennas induces limited angular resolution. Thus, multiple MPCs may appear as one MPC in the view point of an antenna. So, finding the precise number of MPCs in an environment is not trivial. Like in microwave bands, MPCs at mm-Wave bands are likely to occur in clusters. A cluster comprises of rays which come from the same scatterer with similar properties and is typically described by statistical large scale parameters. A scattering environment is depicted in Figure 2.1. One difference that prevents microwave bands channel model to be utilized for mm-Wave bands is the fact that, number of clusters is constant in microwave bands, while for the mm-Wave bands it may not be a proper assumption. Generally, the number of clusters is assumed to be random and small. It can be modeled by the Poisson distribution [45]. In the 3GPP channel model [14], a cluster is described by a joint delay and mean angles, so that the arrival and departure angle of a group of MPCs must be unique and centered around the average propagation delay. The Geometry-based Stochastic Channel Model (GSCM) is a modeling method in which multipath parameters are determined by a probability density function. In this model the ray-tracing principle is used to compute the CIR.

2.4. 3GPP Model for 0.5–100 GHz Specifications and Other Standards

In order to fulfil the 5G networks requirements, future wireless communication will span a frequency range up to 100 GHz where spectrum availability will give access to wide bandwidth channels (up to 2 GHz). The lack of accurate radio propagation models for communication above 6 GHz and their indispensability for 5G technologies development has motivated the study of high frequency channels by the 3GPP and other organizations. In [14], 3GPP highlights the requirements for the new channel model and provides a standard for high frequency communications. Taking into account the sensitivity of the model to the scale of the environment, it investigates four scenarios of interest:

- UMi (Street canyon, open area) modeling scenarios such as a cities or station squares where BSs are below the building height.

- UMa representing rural areas as UMi, but with BSs mounted above rooftop levels of surrounding buildings.
- Indoor (InH) comprising indoor scenarios such as open and closed offices, or shopping malls.
- Rural Macro (RMa) accounting for large and flat rural propagation environments.

For all of the above scenarios, 3GPP provides environment specific path loss models under LoS and NLoS propagation, expression for the probability of having LoS/NLoS , Outdoor to Indoor (O2I) losses and fast fading models. In order to cater for advanced simulations, additional aspects of high frequency communication are considered, such as: the oxygen absorption in the 53-67 GHz interval, angular and delay spread arising with large antennas arrays or large bandwidth, spatially consistent mobility models to investigate scenarios as vehicular communication, blockage models accounting for human and vehicular blockage, ground reflection model and time-varying Doppler shift effect.

2.5. Examples of Available Channels Models

In parallel to 3GPP, other organizations are conducting 5G channel measurements and modeling high frequency channels, among them:

- METIS identified the 5G requirements, performed channel measurements in the 2-60 GHz range and proposed a map-based model, stochastic model and hybrid model [46].
- COST2100 developed a geometry-based stochastic channel model that captures the time-, frequency- and space-dependent characteristic of MIMO channels [47].
- NYU WIRELESexplored 28/38/60/73 GHz bands for both outdoor and indoor channels and proposed modifications or extensions for LoS/NLoS/blockage modeling, wideband power delay profiles and path loss models [9, 48, 49].
- MiWEBA devised a quasi-deterministic channel model addressing shadowing, spatial consistency, environment dynamics, spherical wave modelling, dual mobility Doppler model, ratio between diffuse and specular reflections and polarization [50].
- Fraunhofer Heinrich Hertz Institute developed QuaDRiGa to enable the modeling of MIMO radio channels for specific network configurations, such as indoor, satellite or heterogeneous configurations [51].

3. QuadRiGa Channel Model

QuaDRiGa is used to simulate the radio environment and obtain the CSI of the wireless links in 0.5-100 GHz [51]. The QuaDRiGa model can be categorized as a "statistical ray-tracing model". The term statistical is used due to the fact that scatterers are randomly distributed in the environment. All essential parts of QuaDRiGa are inline with 3GPP-3D model yet a few differences are in the implementation that have no effect on the results obtained on the model. The model contains all essential parts of 3GPP-3D model and is a good option for evaluating 3GPP standardization proposals.

In the new version of QuaDRiGa (v.2) spatial consistency has been added to the channel model in order to accurately assess the performance of mMIMO and multi-cell transmissions. In order to model spatially consistent correlations, the position of scattering clusters must be spatially consistent as well. 3GPP has introduced a modeling approach where the whole set of random variables that determine the location of scattering clusters are spatially correlated [14]. However, this method suffers from the requirement of large amount of memory. In order to reduce the memory requirement, the Sum of the Sinusoids (SOS) method has adopted in QuaDRiGa to model the distance dependent correlation of SSF parameters [52]. In this method relatively small number of sinusoids coefficients are used to generate spatially correlated parameters. Accordingly, the main advantage of this method is simulation speed improvement and low memory requirement.

Here, our focus is on implementing mm-Wave channel model using the QuaDRiGa simulator. A simple scattering environment is depicted in Figure 2.1 where AoD (the angle between transmitter; which is the BS; and scattering cluster) and AoA (the angle between the UE and the scattering cluster) and total path length and resulting delay of path is derived by the model. The model parameters for the frequency range of 450 MHz - 100 GHz with up to 1 GHz bandwidth for different scenarios are defined according to 3GPP 38.901. Each cluster is assumed to have 20 sub-paths (i.e. a single reflection from the scatterer). The sub-paths are used to emulate fading for MPCs. Sub-paths of a cluster are modeled with the same power and delay profiles, this is based on the assumption that the sub-paths from closely clustered paths that originate from the same cluster are unresolvable in the delay domain and have small delay spread [51]. The AoA, AoD, EoA and EoD are different for each sub-path. The coefficients of 20 sub-paths are summed up to create the channel coefficient. A segment is defined as an interval that large scale fading parameters are not changing rapidly. Each segment is several meters long. Inside the segment, the drifting concept [51] is used to traverse the segment and update the delay, angles and phases of MPCs.

Spatial consistency should be seen in both large scale and small scale fading. The spatial consistency ensures that path delays, angles and power change smoothly with space/-time. Typically, large scale parameter are relatively constant over several meters and do not change rapidly. For example, closely located UEs will experience similar large scale fading parameters such as Dealy Spread (DS)s and angular spreads. The changing rate of large scale parameters can be adjusted through "lambda" parameters in the simulator. The small scale fading is affected by the position of scattering clusters. For closely spaced locations, UEs will have both similar DSs and see similar scattering clusters. In fact, QuaDRiGa generates a random process that correlates all random variables used in building the scattering clusters. A decorrelation distance has been defined. It is the distance where for two UEs the correlation of the same variable is below $e^{-1} = 0.36$ and controlled by "SC_lambda". With "SC_lambda=0" the spatial consistency will be disabled. Spatial consistency is evaluated in the literature by investigating the following metrics:

1. The path power along the track for a moving UEs or the powers for nearby UEs. Spatial consistency means that the path powers do not change suddenly, both for LOS and NLOSs components.
2. AoA, AoD, EoA and EoD and the angular spreads along the track.
3. The delays of LOS/NLOS MPCs and the delay spread along the track.

Moreover, we need to emphasize that AoA, AoD, etc... can not be obtained directly from CSI measurement, and it is not recommended to use complex signal processing techniques to find the parameters of MPCs, in this regard, we investigate spatial consistency based on the covariance matrices. The covariance matrix is assumed to be dependent on the user mobility and have a slow variation over time.

3.1. Layout and System Specifications

In order to evaluate spatial consistency feature, QuaDRiGa version 2 is used and the (up-/downlink) MIMO channel based the 3GPP 38.901 UMaNLoS model has generated. The system is operating at 28 GHZ with 200 MHz bandwidth, and 32 BS antennas and 8 UE antennas both with vertical polarization which composing a ULA with omnidirectional element is considered. The orientation of antennas at UE is assumed to be fixed or random. The decorrelation distance of 25 m is chosen (i.e. SC_lambda=25). The number of MPCs is adjusted to be 20, 10, and 5 and each MPC is consist of 20 sub-paths. Simulation settings are detailed in Table 3.1.

Parameter	**Setting**
Simulation Scenario	3GPP 38.901 UMaNLoS
Carrier Frequency	28 GHz
Bandwidth	200 MHz
BS Antennas	ULA consisting of 32 vertically polarized elements
UE Antennas	ULA consisting of 8 vertically polarized elements
UE Antennas Orientation	Fixed/ Random
Number of MPCs	5, 10, 20
Sub-paths	20
Decorrelation Distance	25m

Table 3.1: Simulation settings

3.2. Definition of the Inputs and Outputs and Channel Parameters

Several scenarios are considered where a UE/UEs are moving, on a straight line, circles or randomly. In scenario I, a UE moving in a straight line getting farther from a BS on a track of 20 meters length is considered, see Figure 3.1. The UE position during movement on a straight line with a random direction is starting from [0, 50] m at xy-coordinates and is marked by red triangles. The BS is at xy-coordinates of [0, 0] m. The BS is at a height of 25 m and UE at 1.5 m. We assume transmission from the BS to the UE such that AoA refers to the angles observed at the UE terminal.

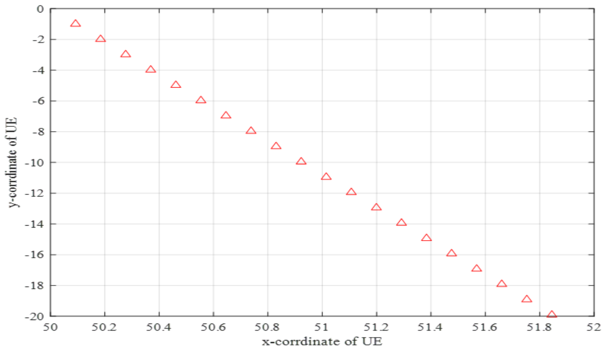

Figure 3.1: A UE moving in a straight line.

Power and delay profiles of the MPCs of the UE along the mobility track are shown in Figure 3.2a. The top figure shows the power profile and the bottom figure shows the delay profile for different clusters as a function of the track samples. The smooth change of power and delay profiles for each cluster are clearly observed. AoD and EoD of MPCs of the UE are depicted in Figure 3.2b. All values are in degree and changing smoothly in each cluster. AoA and EoA of MPCs of the UE are shown in Figure 3.3 for clearness of the figure, the MPCs of few clusters are shown. Based on the power, delay, AoA, EoA, AoD, and EoD profiles of MPCs in the Figures 3.2 and 3.3, the spatial consistency is observed as expected.

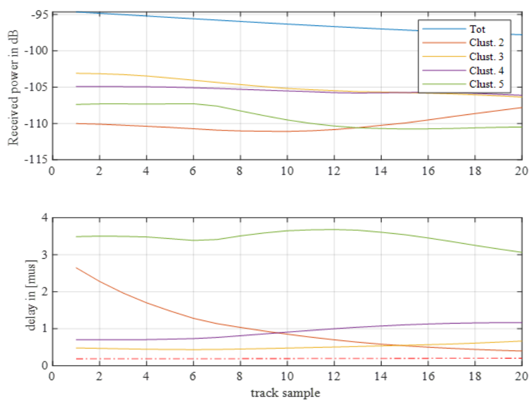

(a) Top: Power profile of MPCs of the UE. Bottom: Delay profile of MPCs of the UE.

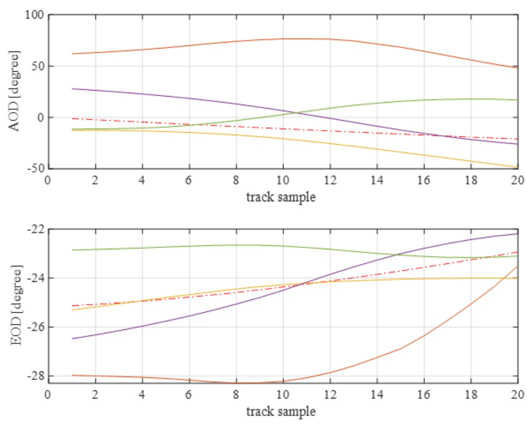

(b) Top: AoD of MPCs of the UE. Bottom: EoD of MPCs of the UE.

Figure 3.2: MPC characteristics of scenario I as a function of track samples.

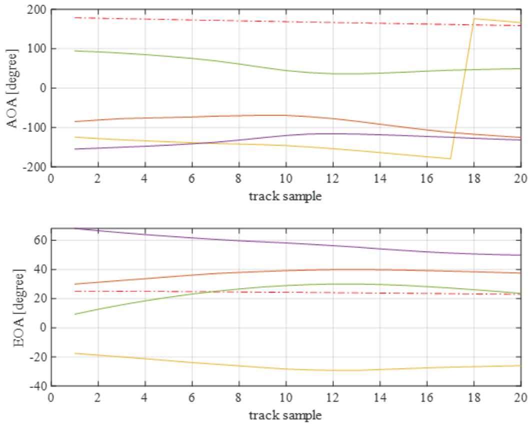

Figure 3.3: Top: AoA profile of MPCs of the UE. Bottom: EoA profile of MPCs of the UE.

4. Ray-Tracing Model

Another approach to model the mm-Wave channel characteristics is to use a ray-tracing channel model. The ray-tracing technique has employed Geometrical Optics (GO) and the Uniform Theory of Diffraction (UTD) [23]. The asymptotic high frequency techniques from GO is often used to analyze wireless propagation. GO is an approximate field measurement method for estimating a high frequency electromagnetic field and when the wavelength of the signal is comparably smaller than the dimension of obstacles in the environment, using the concept of ray propagation is feasible. The GO describes the direct propagation along a straight line path between the TX and the RX, as well as the propagation by reflection from, and the transmission through the surfaces of obstacles that comprise the environment in terms of reflected and transmitted rays. On the other hand, the UTD describes the propagation by diffraction from the edges between two surfaces in terms of diffracted rays [53].
Not only ray-tracing model fills up the gap in stochastic models in preserving spatial consistency , but also provides good agreement with field measurement results as discussed in [54]. By virtue of availability of 3D geometrical information [55] various urban scenarios have been modeled based on ray-tracing models. The 3D structure of downtown areas are modeled and then 3D ray-tracing simulations at a given frequency (e.g. 28 GHz) are performed.
At first, the pathloss propagation of ray-tracing model is compared to a reference model (e.g. 3GPP standardization group). Then, the channel model provides crucial channel parameters such as shadowing as well as delay, angle, and elevation spreads. In [56], authors have provided a dual slope pathloss model for downtown Ottawa. Dual slope model corresponds to a model which provides two different pathloss formulas and shadow fadings values for different range distances. The dual slope model fits well with measurement campaigns which means lower root mean square error between simulation results and model output.
sectionMathematical Model In [4], a ray-tracing mm-Wave cellular channel model was created following the principles of [55]. The channel simulator models the path loss experienced by the multi-path components using the free-space path loss model with power inversely proportional to the square of the distance. The reflections from obstacles, i.e. the walls, are modeled such that the reflection coefficients are based on Fresnel's equations. The typical value for the wall relative permittivity is between 4 and 6. The channel for each link is then calculated using the ray-traced paths with the path loss, reflection losses and antenna gain accounted for in the channel. The multipath gain $\beta_{b,k}^{(l)}$ is computed as:

$$\beta_{b,k}^{(l)} = e^{i\psi_l}\sqrt{G_0 \rho d_l^{-2} g_1(\theta_l) g_2(\phi_l) \prod_{i=1}^{R} |r_l^{(i)}|^2}, \tag{4.1}$$

where $G_0 = 10^{-6.14}$ is the omnidirectional path gain at a reference distance of 1 m, ρ is the transmit power, ψ_l is the phase modeled as a uniform random variable $\psi_l \sim \mathcal{U}(0, 2\pi)$, d_l is the propagation distance in meters, $g_1(\theta_l)$ and $g_2(\phi_l)$ are the antenna gain for an angle of departure θ_l at the UE and angle of arrival ϕ_l at the BS, respectively, R is the number of reflections that the lth multipath component undergoes, and $r_l^{(i)}$ is the i^{th} reflection coefficient. For a LOS path, $R = 1$ and$r_l^{(1)} = 1$.
In order to create sub-rays within a cluster, according to the 3GPP standards [14], after the cluster generation, the following steps needed to be taken. To do so, as an example we need

to generate arrival and departure angles for both azimuth and elevation. AoA for cluster n and AoA for ray m in cluster n are defined as $\phi_{n,AOA}$ and $\phi_{n,m,AOA}$ respectively. The composite Power Angular Spectrum (PAS) in azimuth of all clusters is modeled as wrapped Gaussian. The AoAs are determined by applying the inverse Gaussian function with input parameters P_n and RMS Azimuth Spread of Arrival angles (ASA) as:

$$\phi'_{n,AOA} = \frac{2(ASA/1.4)\sqrt{-ln(P_n/max(P_n))}}{C_\phi}, \tag{4.2}$$

where P_N is the power of cluster n , and C_ϕ is defined as:

$$C_\phi = \begin{cases} C_\phi^{NLOS}.1.1035 - 0.028K - 0.002K^2 + 0.0001K^3 & \text{for } LOS, \\ C_\phi^{NLOS} & \text{for } NLOS, \end{cases} \tag{4.3}$$

where K is the Ricean K-factor, C_ϕ^{NLOS} is defined as a scaling factor related to the total number of clusters and is given in Table 4.1.

#clusters	4	5	8	10	11	12	14	15	16	19	20
C_ϕ^{NLOS}	0.779	0.860	1.018	1.090	1.123	1.146	1.190	1.211	1.226	1.273	1.289

Table 4.1: Scaling factors for AoA, AoD generation

In the LOS case, constant $C_\phi$also depends on the Ricean K-factor K in [dB]. Additional scaling of the angles is required to compensate for the effect of LOS peak addition to the angle spread. Assign positive or negative sign to the angles by multiplying with a random variable X_n with uniform distribution to the discrete set of $\{1, -1\}$, and add component $Y_n \sim \mathcal{N}(0, (ASA/7)^2)$ to introduce random variation

$$\phi_{n,AOA} = X_n\phi'_{n,AOA} + Y_n + \phi_{LOS,AOA}, \tag{4.4}$$

where $\phi_{LOS,AOA}$ is the LOS direction defined in the network layout description, see Step1c. In the LOS case, substitute (4.4) by (4.5) to enforce the first cluster to the LOS direction $\phi_{LOS,AOA}$

$$\phi_{n,AOA} = (X_n\phi'_{n,AOA} + Y_n) - (X_1\phi'_{1,AOA}Y_1 - \phi_{LOS,AOA}), \tag{4.5}$$

Finally add offset angles $\alpha_m$from Table 4.2 to the cluster angles:

$$\phi_{n,m,AOA} = \phi_{n,AOA} + c_{ASA}\alpha_m, \tag{4.6}$$

where c_{ASA} is the cluster-wise RMSE ASA (cluster ASA). The generation of AoD follows a procedure similar to AoA as described above.

4.1. Layout and System Specifications

In the ray-tracing approach, 3D geographical building models are utilized to model urban environments. The downtown area of New York City is modeled according to [5]. In our scenario , 10 BSs, 6 streets and 5000 UEs are considered. The UE locations are randomly generated on the streets of a Manhattan grid.The simulation parameters are shown in Table 4.3. The UE locations are generated on the streets of a Manhattan grid as shown in Figure 4.1.

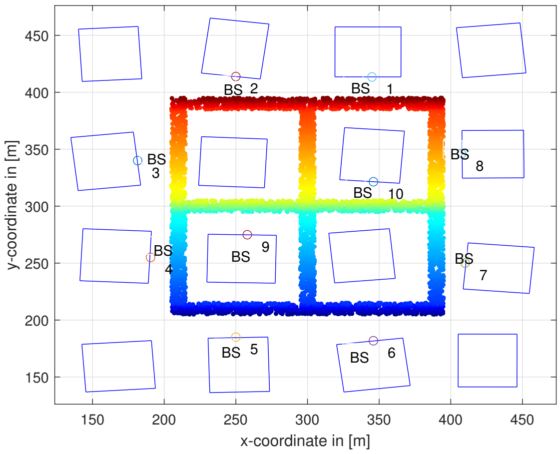

Figure 4.1: Simulated scenario: Streets in a Manhattan grid with 10 BSs labeled by numbers and sampled UE locations marked by colors.

4.2. Definition of the Inputs and outputs and channel parameters

A scenario showing the propagation paths for multipath components using the ray-tracing model is shown in Figure 4.2. A UE location has LOS communication with one BS (BS-LOS) and a NLoS communication with another BS (BS-NLOS). The SNR observed at BS-LOS which is at a distance of 43.01 meters is obtained as 38 dB. The SNR at BS-NLoS which is at a distance of 235.7 meters is calculated as -36.83 dB.

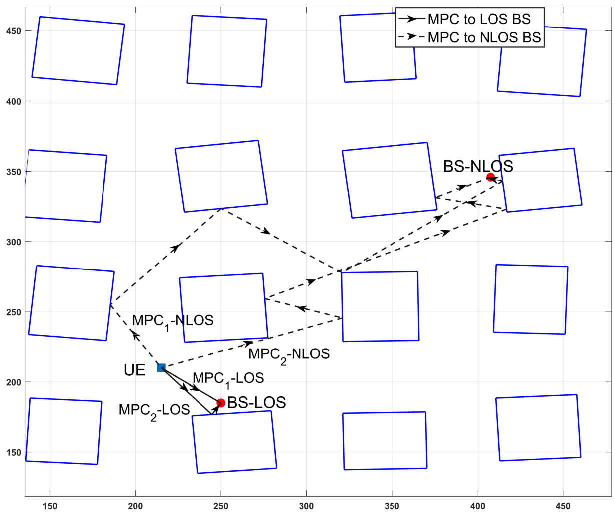

Figure 4.2: A scenario showing the propagation paths and MPCS for a UE location with LOS and NLOS BSs.

As another example of ray-tracing model, an urban outdoor multi-cell mm-Wave scenario is considered. Figure 4.3 shows rays from one UE location at [218, 205] xy coordinate to BS 7 in a NLOS scenario in order to have a clear observation of transmitting rays. It is a suitable scenario to see LOS, NLOS locations and a handful of applications could be considered to

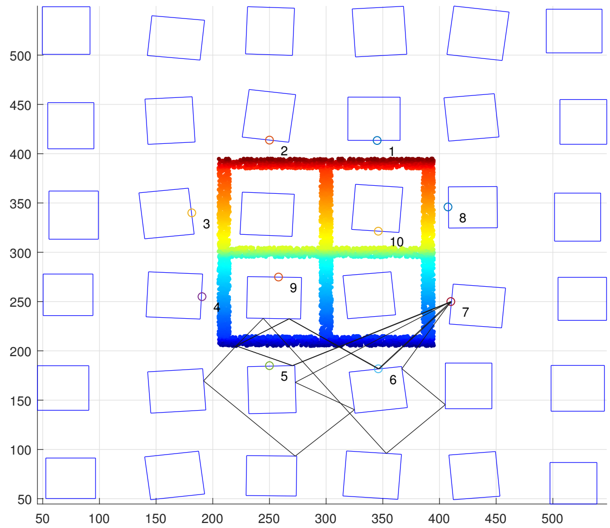

Figure 4.3: NLOS scenario. Streets in a Manhattan grid with 10 BSs labeled by numbers and sampled UE location at [218, 205] xy-coordinate.

evaluate. For instance, it can be used for beamformer at street cross sections handover from a BS to another, for Vehicle to Vehicle (V2V) communications, and positioning.
Figure 4.4 is an illustration of a 3D ray-tracing model. UEs are located in the red street (i.e. starts from the location [150, 125] at xy-coordinates, turns 90° at [450, 125], and ends at [450, 325]) , BS is located at [320, 180]. Location information of UEs and BS could be found in Table 4.4. Figure 4.4 shows the received signals from all UEs, each color represents received signal from a different group of UEs at the BS. In other words, each color corresponds to a cluster from which the UEs' signal is reflected. Thus, by using ray-tracing model the relevant clusters are geometrically found. Such results could further used in beamforming and handover problems.

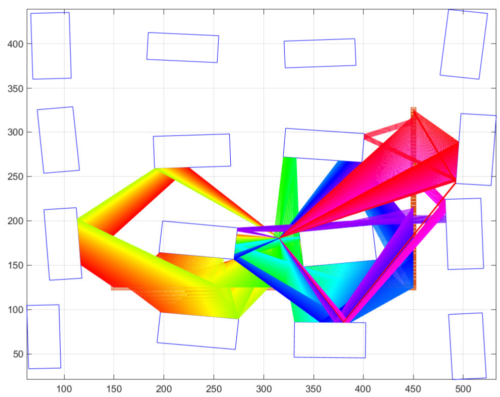

Figure 4.4: Received rays of all UEs at the BS.

Ray number m	**Basis vector of offset angles** α_m
1,2	± 0.0447
3,4	± 0.1413
5,6	± 0.2492
7,8	± 0.3715
9,10	± 0.5129
11,12	± 0.6797
13,14	± 0.8844
15,16	± 1.1481
17,18	± 1.5195
19,20	± 2.1551

Table 4.2: Ray offset angles within a cluster, given for Root Mean Square Error (RMSE) angle spread normalized to 1

Parameter	**Value**	**Parameter**	**Value**
Pathloss at 1 m	61.4 dB	Reflection loss	0-15.5 dB
UE TX power	23 dBm	BS noise power	-86 dB
BS antenna gain	0 or 2	UE antenna gain	1
Bandwidth	200 MHz	OFDM subcarriers	256
BS antenna	64 ULA	UE antenna	8 ULA
BS array gain	18 dB	UE array gain	8 dB
Noise figure	6 dB	Noise power	-174 dBm
Num. of subrays/cluster	5	Max. num. of bounces	5
Max. num. of multipaths	10	Intra cluster mean delay	10 ns

Table 4.3: Simulation settings [55]

BS/UE	BS location	UEs' starting point	UEs' turning point	UEs' ending point
xy coordinate m	[320, 180]	[150, 125]	[450, 125]	[450, 325]

Table 4.4: Locations of UEs and BS of Figure 4.4

5. System Performance Evaluation

We are interested in deducing whether two users in a cellular system are at nearby physical locations from measuring similarity of their covariance matrices at a base station. This requires, first of all, a spatially consistent channel model. Even if a consistent model is available, there are challenges in MIMO mm-Wave channels, as the semi-optical nature of mm-Wave radio propagation gives rise to non-Kronecker correlation.

5.1. QuadRiGa channel generation

In order to estimate the channel at the BS from a UE transmission, the UEs may transmit, e.g., a known pilot sequence $\boldsymbol{x}(t)$ of dimension r weighted by a beam matrix $\mathbf{W} = [\mathbf{w}_1, \dots, \mathbf{w}_r]$. Depending on the UE hardware architecture, $\mathbf{W}$ may be transmitted with analog or fully digital beams. The selection of $\mathbf{W}$ can be expressed as $\mathbf{W} = \boldsymbol{\Omega}\big(\{\boldsymbol{H}(t)\}_t\big)$, where $\boldsymbol{\Omega}$ is a function which takes the instantaneous channel state, or the measured covariance information as an input, and gives a precoder as the output, normalized as $\mathrm{Tr}(\mathbf{W}^H\mathbf{W}) = 1$. We assume that the pilot vector is transmitted well within channel coherence time. The received signal vector $\boldsymbol{y}(t) \in \mathbb{C}^{M\times 1}$ at the BS is given

$$\boldsymbol{y}(t) = \boldsymbol{H}(t)\mathbf{W}\boldsymbol{x}(t) + \boldsymbol{z}(t), \tag{5.1}$$

where $\boldsymbol{z}(t) \in \mathbb{C}^{M\times 1}$ is the additive Gaussian noise with zero-mean. The BS may have a fully digital, or hybrid beamforming architecture. If the BS is fully digital, it may estimate $\boldsymbol{H}(t)\mathbf{W} \in \mathbb{C}^{M\times r}$ from the pilot transmission. In a hybrid architecture, the BS will not be able to individually measure the received signal at different antennas. However, if similar measurements are performed with multiple different analog Rx-beams, the BS will be able to reconstruct the full M-dimensional channel from the knowledge of the measurements, and the dictionary of analog beams used for the measurements [9]. Accordingly, it is reasonable to assume that the BS can estimate $\boldsymbol{H}(t)\mathbf{W}$ with reasonable accuracy, if a sufficiently long pilot sequence is used, irrespective of the BS array architecture.
The non-Kronecker covariance structure of mm-Wave channels of the equation (2.4) implies that care has to be taken when determining the signal covariances $\boldsymbol{Q}_{UE}$, if similarity of user locations is to be deduced from the covariance matrices. If transmissions from different UEs in the same large scale fading environment are to be identified to come from nearby locations, a coordinated principle for selecting transmission covariances $\boldsymbol{Q}_{UE}$ is needed.
We consider the problem of designing the precoder selection function $\boldsymbol{\Omega}$, aiming to preserve spatial consistency of a set $\mathcal{U}$ of UEs moving in a radio environment characterized by the same large scale parameters and scatterers. The spatial consistency of a pair of UEs $u, u' \in \mathcal{U}$ in the radio environment can be measured, e.g., by the $d_{CMD}\big(\boldsymbol{R}_u, \boldsymbol{R}_{u'}\big)$, where $\boldsymbol{R}_u = \boldsymbol{R}_u[\boldsymbol{\Omega}]$ is the estimated covariance of UE u at the BS, when precoder selection principle $\boldsymbol{\Omega}$ is used. For a Kronecker channel model, the CMD would not depend on $\mathbf{W}$ at all, while for non-Kronecker channel models it does depend. Thus we will have to address the selection of $\boldsymbol{\Omega}$.
The precoder design problem can be formulated based on CMD as:

$$\min_{\Omega} \sum_{u\neq u'} d_{CMD}\big(\boldsymbol{R}_u, \boldsymbol{R}_{u'}\big). \tag{5.2}$$

Solving (5.2) is not analytically tractable. We consider two families for determining Ω; UE-side covariance based and instantaneous UE CSI based beamformers. For covariance based UE pilot beamformers, V largest eigenvalue eigenvectors are considered. For instantaneous CSI based beamformers, V largest singular value singular vectors are considered. The effect of the rank V on the average pairwise CMD for covariance/instantaneous based UE pilot beams is evaluated using simulations in the next section.

5.2. QuadRiGa Settings

As an example, we consider a 3GPP 38.901-UMaNLoS mm-Wave radio environment with 28 GHz carrier frequency, 200 MHZ bandwidth, 256 subcarriers and 20 clusters each with 20 rays. We consider the scenario I with a 32-antenna BS placed at $[0, 0, 10]$ m and 20 UEs, each having 8 antennas. UE 0 is located 50 m from the BS and UEs $u = 1, \ldots, 19$ are on a straight line separated by a distance of 1 m from each other. To create covariance estimates, 50 spatial fast fading samples are generated for each UE within a uniform distance of 1 m. Noiseless covariance estimation is assumed. The CSI is generated using the QuaDRiGa channel simulator [51]. Figure 5.1, shows the CMD of UE 1 with respect to the other users for different ranks of the covariance based UE pilot beamformer. The CMD reduces with increasing rank, as expected. Thus, spatial consistency (similarity/dissimilarity) can be captured more accurately using a UE pilot beamformer with a higher rank.

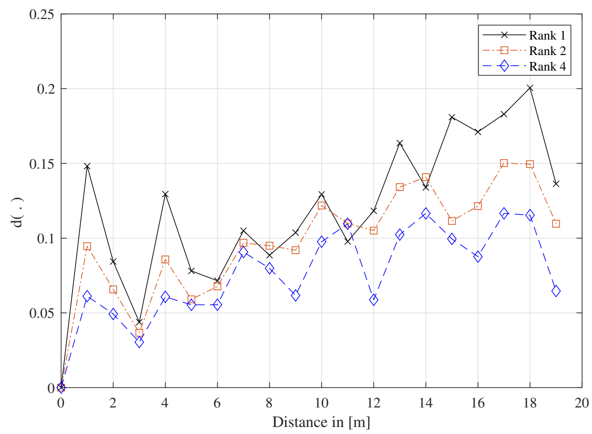

Figure 5.1: The CMD as a function of the distance between UE 1 and u for different ranks of the covariance based UE pilot beamformer in a noiseless scenario.

In the scenario II, 20 static UEs are evenly located on the circumference of a space of radius 5 m and are indexed from 1-20 in counter clock wise manner as well as the BS is at origin $[0, 0]$, see Figure 5.2. Like in scenario I, all performance metrics (i.e. the power, delay, AoA, EoA, AoD, and EoD profiles of MPCs of UEs) are considered, showing the spatial consistency is captured. Each cluster parameter (power, delay, AoA, EoA, AoD, and EoD profile) evolves continuously and smoothly as it can be observed in Figure 5.3. Figure 5.3a shows power and delay profiles where nearby users have almost the same received power. Figure 5.3b shows that the AoD, and EoD profiles change smoothly for different clusters as a function of UE index.

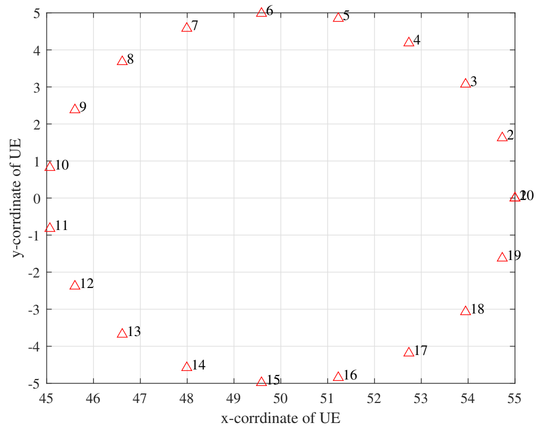

Figure 5.2: Static UEs on the circumference of a circle.

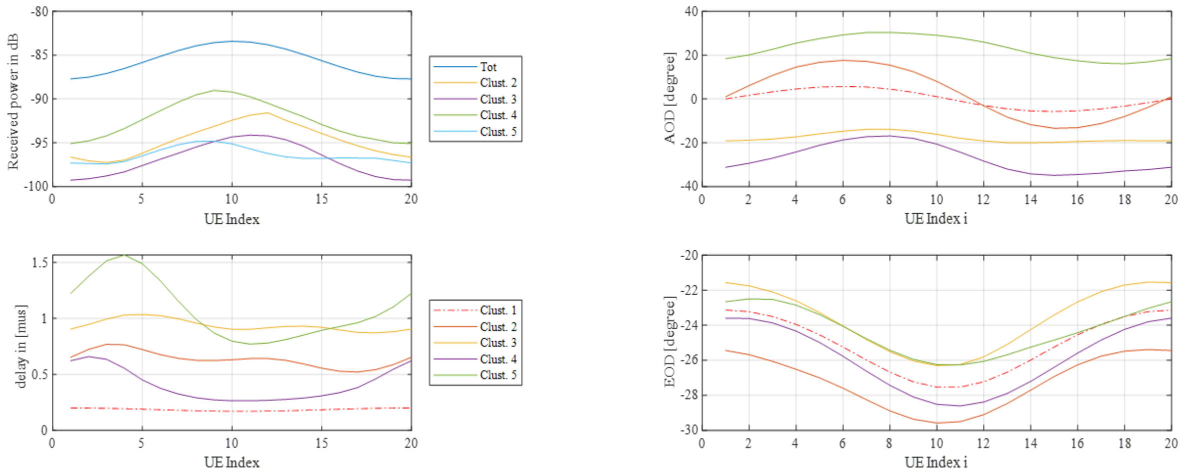

(a) Top: Power profile of MPCs of UEs. Bottom: Delay profile of MPCs of UEs.

(b) Top: AoD profile of MPCs of UEs. Bottom: EoD profile of MPCs of UEs.

Figure 5.3: MPC characteristics of scenario II as a function of UE index.

In retrospect to the scenario I, different similarity measures has been applied to the covariance matrix of UE at first track sample and other parts of the track. Figure 5.4a shows the CMD and chordal distance as a function of track sample. The variations of the CMD and chordal distances as a function of track sample are not smooth. Figure 5.4b shows the CMD and chordal distance as a function of UE index for scenario II. UE 1 is the reference point for measurements. Likewise, variations of the CMD and chordal distances are not smooth and it is due to the fact that, the obtained results were based on a single spatial sample. Hence, it is difficult to reveal the spatial consistency of the environment. However, the spatial consistency is well captured in this scenario where small chordal and CMD distance is obvious for UEs in vicinity of the UE 1. It worth mentioning, chordal distance is not a normalized distance measure and the value range is a function of the power of channel coefficients.

To capture the spatial consistency (i.e., smooth behavior) of the measurements at the BS based on covariance matrices we consider the long-term average covariance matrix (aver-

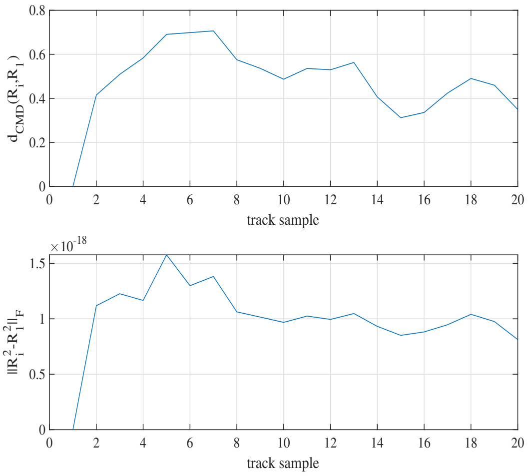

(a) Top: CMD distance. Bottom: Chordal distance. As a function of track sample.

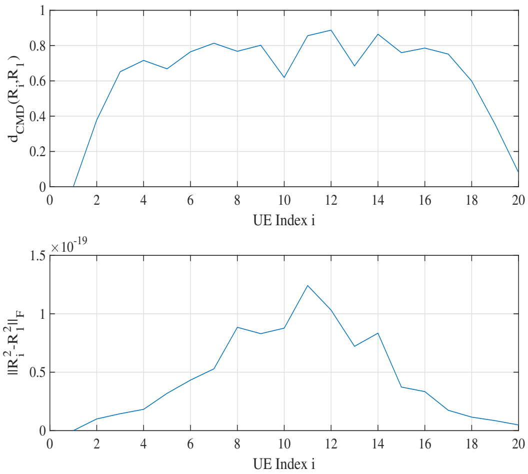

(b) Top: CMD distance. Bottom: Chordal distance. As a function of UE index.

Figure 5.4: Covariance matrix measures. Left: Scenario I. Right: Scenario II.

aged over several spatial samples) and then compute the CMD and chordal distances. In addition, covariance and instantaneous based pilot beamformer are considered to deal with non-Kronecker mm-Wave channel in scenario III. Figure 5.5 shows a sample environment where 20 UEs are scattered in an area of 10×10. We create 20 environments. An environment is determined by a set of AoAs and AoDs. Each UE moves in a random direction for 1 m. The movement of UE 1 is shown. The number of snapshots is 100 and the BS is at xy-coordinates $[0, 0]$ m. The UEs may transmit either with estimated covariance matrix, 1-8 eigenvectors, or instantaneous right singular vectors, 1-8 of them. A covariance matrix is estimated for each of the UEs in the environment Here, we have adopted the mean CMD of the environment as a measure of spatial consistency. The mean CMD between the estimated covariance for each method is computed in each environment.

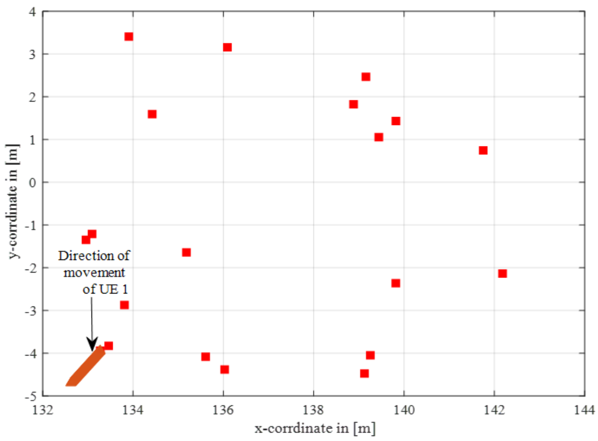

Figure 5.5: A population of 20 UEs.

Figure 5.6 shows the average CMD by considering instantaneous and covariance based pilot beamformer of different ranks for different MPCs (rank represent the number of ordered

Eigen vectors or singular vectors). The CMD value is affected by the number of MPCs in the environment. It reveals that, there is an optimum rank. Increasing the rank beyond this increases the noise contribution more than improves the covariance similarity. The reason for this is that with increasing rank, the overall received signal power is reduced, such that the noise component in the covariance estimate increases.

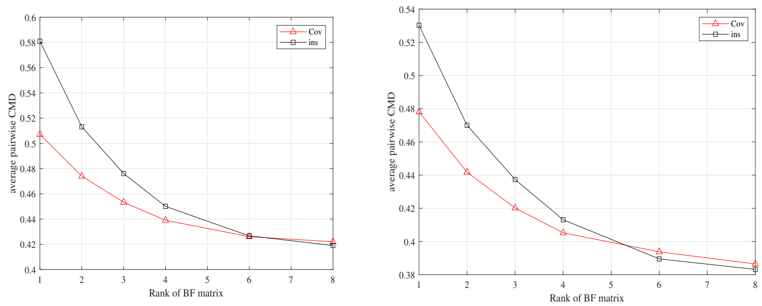

(a) Environment with 20 MPCs. (b) Environment with 10 MPCs. (c) Environment with 5 MPCs.

Figure 5.6: Average CMD as a function of beamformer rank.

Figure 5.7 shows how the average CMD value is effected by the number of antennas in the same environment with 20 MPCs. The number of antennas has changed from a 32 antenna ULA to 16 and 8 antenna ULA. The size of the environment also has an effect on the average pairwise CMD. Figure 5.8 shows how CMD value changes in a smaller area of 5 $\times$ 5 as compared to a larger area with the same number of MPCs (20 MPCs). From all observations it is concluded that in order to have spatial consistent measurements the rank of the covariance and instantaneous based pilot beam former needed to be designed.

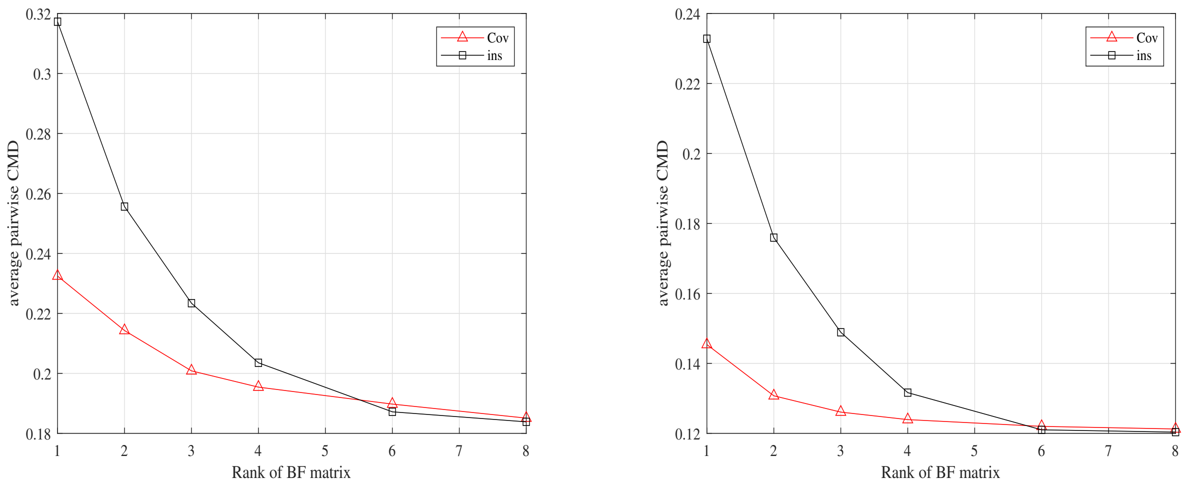

(a) 16 antennas at BS. (b) 8 antennas at BS.

Figure 5.7: Average CMD as a function of beamformer rank. Environment contains 20 MPCs.

In scenario IV and V, moving of UEs on straight line and their random movement in the environment is considered and the effect of that on the average CMD has been shown.

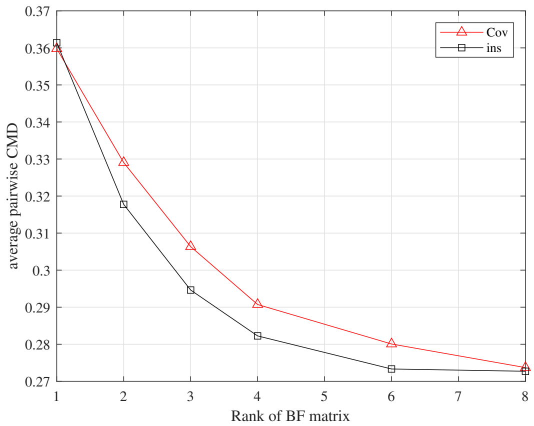

Figure 5.8: Average CMD as a function of beamformer rank. The environment size is 5×5.

Figure 5.9a shows UEs are moving on straight lines of 5 m long. A different antenna orientation for each UE is considered and all UEs pass the center point. To create covariance estimates,100 time domain snapshots are generated for each UE. Figure 5.10 shows the average CMD by considering instantaneous and covariance based pilot beamformer of different ranks. Figure 5.10a depicts the average CMD value for an environment of diameter 5 m with 20 MPCs whereas Figure 5.10b exhibits the CMD value for an environment of diameter 1 m with the same number of MPCs. The average CMD can be used to measure the spatial consistency of the environment as indicated by the small values of the CMD as shown in Figure 5.10 for UEs passing through the same center point.

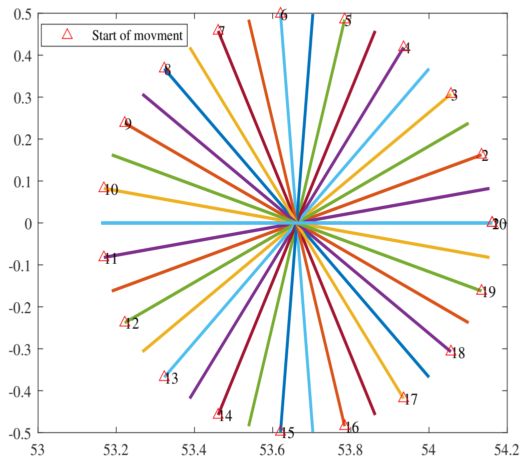

(a) Movement on straight lines.

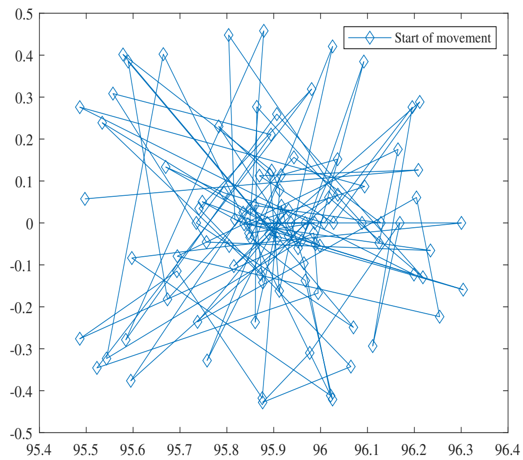

(b) Random movement.

Figure 5.9: Movement of a population of 20 UEs. Left: Scenario IV. Right: Scenario V.

In scenario V, UEs are moving on random directions. Different antenna orientation is considered at each track sample and this scenario is constructed based on random samples from the track positions of the whole population as shown in Figure 5.9b. The average CMD value by considering instantaneous and covariance based pilot beamformer of different ranks for environments of 5 m and 1 m diameter are shown in Figure 5.11a and 5.11b respectively. If

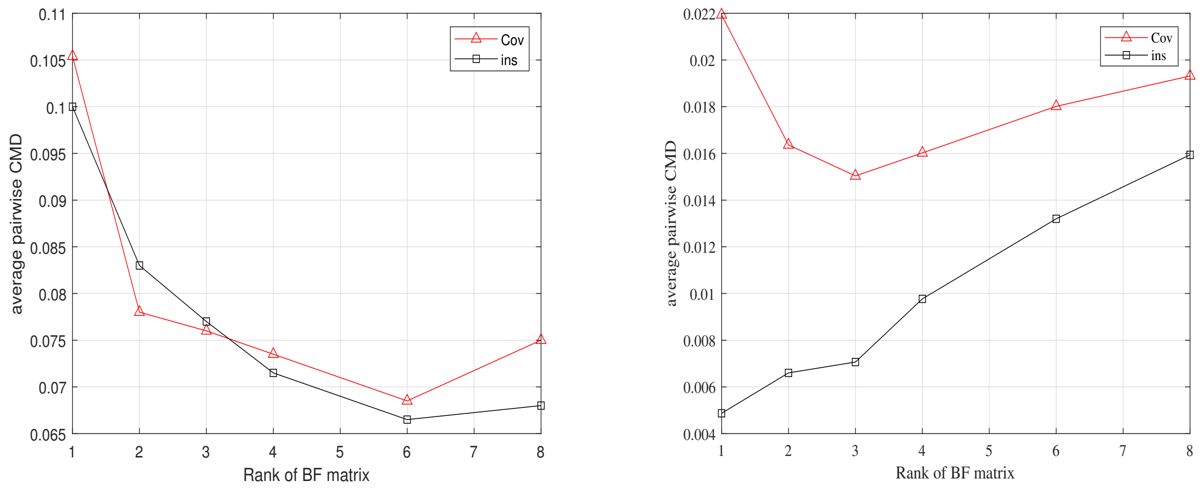

(a) The environment diameter of 5 m. (b) The environment diameter of 1 m.

Figure 5.10: The average pairwise CMD for the movement passing the center point.

we have the chance to sample the environment randomly with different antenna orientations, the average CMD computed based on covariance based pilot beam former has the capability to reveal the spatial consistency of the environment. Figure 5.11b shows the CMD based on instantaneous pilot beam former with rank 1 gives better CMD compared to higher ranks.

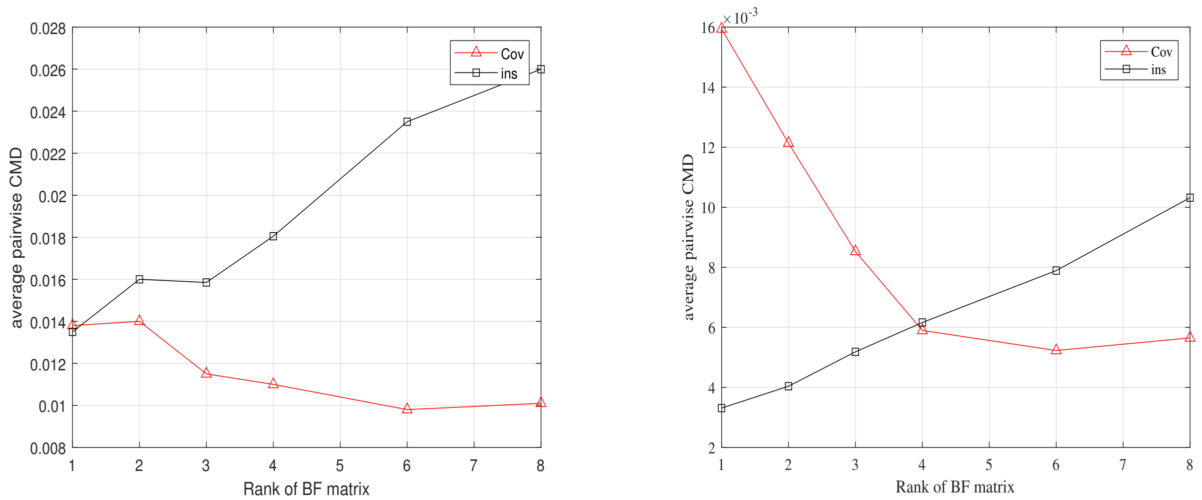

(a) The environment diameter of 5 m. (b) The environment diameter of 1 m.

Figure 5.11: The average pairwise CMD for random movement.

5.3. Ray-Tracing Channel Generation

In order to investigate performance of the ray-tracing simulator, we used the ray-tracing channel simulator to model channels between UEs and BSs. Then, we consider a machine learning algorithm to predict the SNR of a user transmission at neighboring base stations in a mMIMO cellular system. This information is needed for HO decisions for mobile users. For SNR prediction, only uplink channel characteristics of users, measured in a serving cell, are used.

Large-scale effects of wireless channel are caused by reflection, diffraction, and scattering of the physical environment, whereas small-scale effects are caused by multipath propagation and related destructive/constructive addition of signal components. The CC is based on the assumption that statistical properties of MIMO channel vary relatively slowly across space, on a length-scale related to the macroscopic distances between scatterers in the channel, not on the small fading length-scale of wavelengths. In this regards, the CSI covariance matrix can be used to capture large-scale effects of the wireless channel based on the assumption that there is a continuous mapping from the spatial location of a UE to the covariance CSI.

CC starts by processing the CSI covariance matrix into suitable channel features that capture large-scale properties of the wireless channel. CC then proceeds by using a set of collected features for a set of UEs seen by a BS to learn a dissimilarity matrix. Different approaches can used to select the channel features and then computing the dissimilarity matrix (see, [2, 4]). However, we select the feature vector based on multi-path components. These multipath component parameters are estimated from the covariance matrix using the multiple-signal-classification (MUSIC) algorithm. Next, MPCs are clustered. The dissimilarity between two UEs is based on identifying MPCs in their feature vectors that are similar [5]. Thus, dissimilarity coefficient between a pair of UEs is computed taking into consideration MPCs of the UEs that are in the same cluster. Multipoint channel charting utilizes the different views of the spatially distributed BSs by fusing the BS-specific dissimilarity matrices into a global dissimilarity matrix [4].

Radio maps can be utilized for RRM functionalities. To construct radio maps, either the physical or the logical location of the UEs in the radio environment and the corresponding CSIs are needed. The physical location can be obtained either by a Global Navigation Satellite System (GNSS) such as GPS. CC can be used with a single BS, however, using more BSs improves the CC accuracy. CC has the advantage of replacing the timely and costly measurement campaign in GNSS fingerprinting based algorithms by heavily processing ML algorithms (i.e., unsupervised learning plays a key role of mapping radio features to logical locations and preserving neighborhood relations) at the BSs, which has the advantage of being able to be applied for large scale areas and in an automated manner when the radio environment changes. The back-haul cost of CC is less than the back-haul of GNSS fingerprinting, since the location information is not transmitted. To use a channel chart for RRM functionalities, new UEs can be added to an existing CC based on their radio frequency CSI (i.e., covariance matrix) as in [57]. Then, from a CSI measurement of a new UE, possible CSI states can be predicted, by comparing to the CSI of nearby positions in the chart.

The HO process is a core element of cellular networks to support user mobility. HO management has always been a central research area in the context of cellular networks (see [58] for GSM/CDMA). HO is the process of changing the UE serving BS with mobility such that the best BS is always selected. A simple rule for selecting the best BS is based on the average Received Signal Strength (RSS) level, i.e., the UE changes its association if another BS provides a higher RSS than the serving BS, which may happen when the user moves away from the serving BS towards another BS.

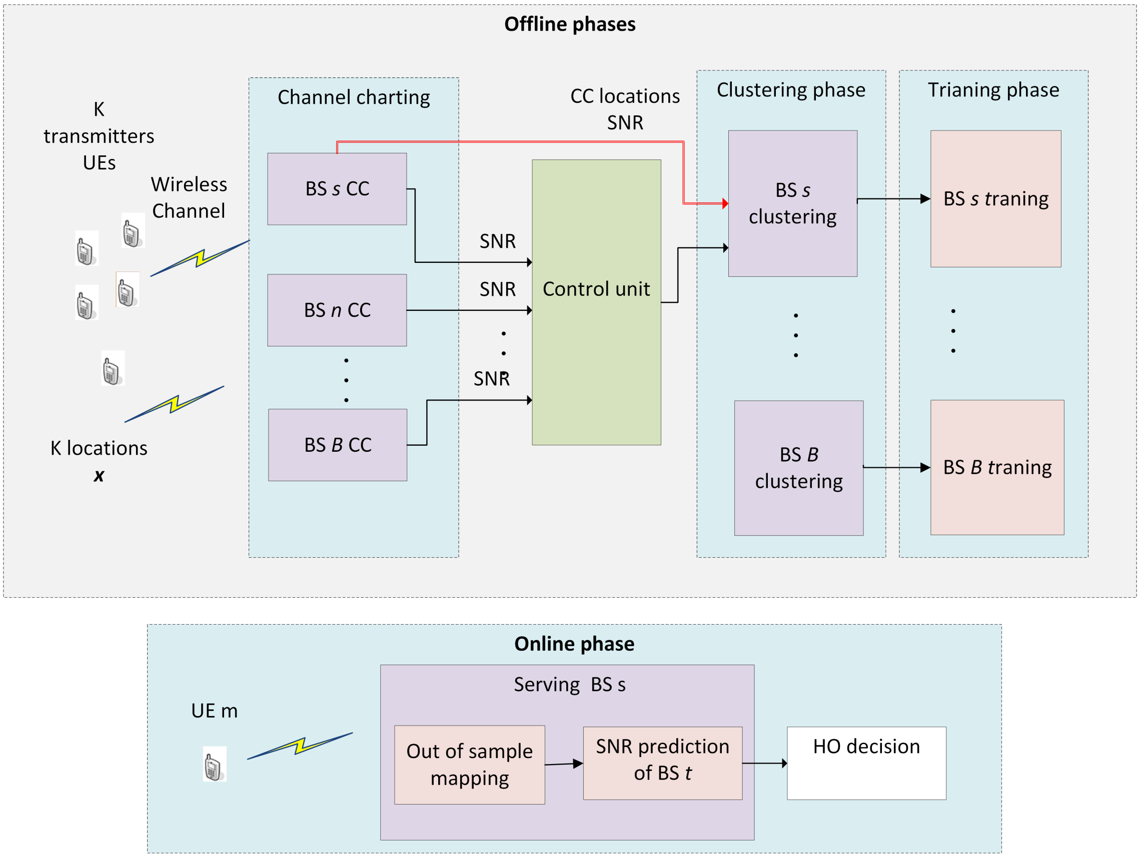

Figure 5.12: The principle of Channel Charting based Network Controlled handover.

Path losses at mm-Wave bands can be overcome by the use of mMIMO systems. In mm-Wave cellular systems, the BS transmits multiple narrow beams towards the UE. Beamformed transmissions over different beams (up to 64 beams) are allowed in 5G-NR for mm-Wave frequencies. In this architecture, a new handover (beam switching) within the same BS or among different BSs can occur. We consider that the UE has one transmitting antenna, the UE pilot signal is received at the serving BS and used for SNR predication at neighboring BSs based on CC for handover management.

Channel Chart-based-Network-Centric-Handover (CCNCH) is based on the large scale radio features of a UE, measured at the serving BS. The serving BS has a channel chart, constructed offline, where the CC locations are annotated with measured SNR values of the neighboring BSs, and a prediction algorithm to predict the SNR of a neighboring BS. During online operation, the annotated CC, and the SNR prediction algorithm are used for making HO decisions for a new population of users. CCNCH is a distributed algorithm that is implemented at each BS. It is illustrated in Figure 5.12.

The input of CCNCH training is a set of measurements from UEs, collected in a short enough time scale such that the UE is in the location from the point of view of large scale channel characteristics. All BSs in the network that are able to detect the UE, measure the UE channels, and construct a received SNR from the UE. These measurements represents samples from the continuous function of radio signals from the *s*-dimensional spatial coverage area of the network to radio feature space.

Offline training consists of three phases: channel charting, annotation, and training of SNR

map. In the online phase, the developed SNR mapping functions will be used by a BS (e.g. BS s) to predict the neighbor-cell SNRs of a mobile user that it serves. The prediction is solely based on received signal measurements at the BS s.
Based on the annotated channel chart $\mathcal{C}_s^{(t)}$, BS s should find the function $g_s^{(t)}$ that predicts the SNR γ_t at target cell t for a transmission at any CC location and received SNR $\gamma_{s,m}$. We shall use machine learning methods to find this function. We consider dB-valued SNRs both at input and output, to have the dynamic range of the variables under control, and take the cost function to be minimized in training to be prediction Mean Squared Error (MSE). We consider three learning algorithms for prediction; GPR, a Support Vector Machine (SVM), and NN.
We compare GPR and SVM to a NN based regression function. For this, we consider a fully connected neural network, with three real-valued inputs, a number of hidden layers, and one real-valued output, providing the SNR prediction. For the learning process, forward and backward propagation phases are applied. First, weights are initialized randomly. In the forward phase, the input is fed to the network through input neurons, and is propagated across the hidden layers until the output layer. The error between the predicted output and the given output from the input data is calculated. Then, in the backward phase, based on the error, we use the Levenberg-Marquardt method to adjust the weights and biases so that the output MSE is minimized. We split the data set randomly into three sets; 80% is used for training, 10% for validation and 10% for testing. To avoid overfitting, during training, the performance is tested against the validation set. Once the validation error is larger than the training error for six consecutive iterations, we backtrack to the weights that provided the smallest validation error. Prediction results are then provided for the testing set.
The prediction accuracy of a NN depends on the weight initialization; depending on initialization, the NN may converge to different local optima. To mitigate this, we use several random initializations to generate multiple NN predictors. The NN that provides the best performance on the validation set is selected.

5.4. Ray-Tracing Setting

An urban outdoor multi-cell mm-Wave scenario is considered as discussed in [2]. The system parameters are shown in Table 5.1. A ray-tracing channel model is used to generate multi-path channels. The UE locations are randomly generated on the streets of a Manhattan grid. The CSI of the UEs are estimated at multiple BSs.

Parameter	Value	Parameter	Value
Carrier frequency	28 GHz	Bandwidth	256 MHz
UE TX power	23 dBm	BS noise power	-86 dBm

Table 5.1: Simulation parameters [2]

First, to get a gist of CCNCH in a multicellular environment, we consider a scenario with 10 BSs, 6 streets and 5000 UEs. A channel chart based on Laplacian eigenmaps is generated as shown in Figure 5.13. Each UE in this figure is colored based on its best BS. For comparison, the ground truth location of UEs and BSs are also shown.

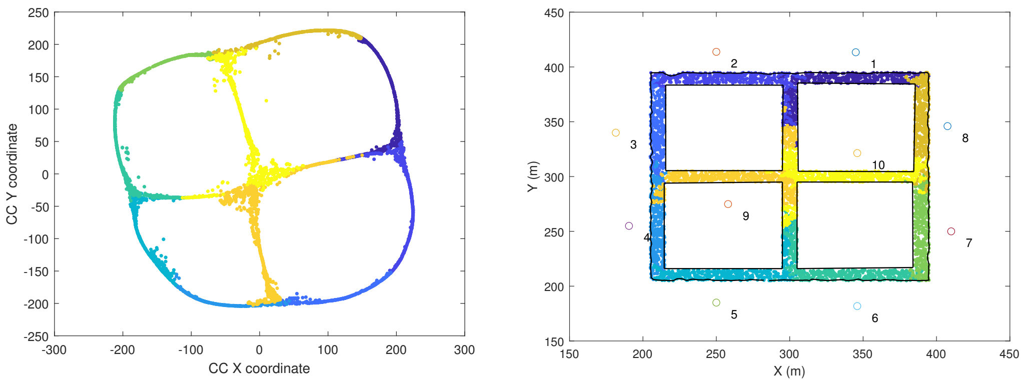

Figure 5.13: Channel charting for a 10 BS network. Left: CC. Right: Ground truth spatial location in Manhattan Grid. Each color is associated to UEs that are served by a BS. BS locations indicated by numeric labeled circles.

For each of the BSs $s = 1, \dots, 10$, we construct CC groups $\mathcal{G}_s^{(t)}$ for handover target cells $t \in \mathcal{T}_s$ so that $\mathcal{G}_s^{(t)}$ consists of the UEs for which the two best BSs are s and t in any order. The SNR mapping function to predict the target BS t in each group $\mathcal{G}_s^{(t)}$ $s = 1, \dots, 10$ and $t \in \mathcal{T}_s$ is then created. NN, GPR and SVM predictors are used.
For GPR, we select the exponential kernel, since it has the best performance compared to other kernels functions for the data set. A NN with three hidden layers with 10 neurons each is used.
The RMSE of the predictors are measured. The standard deviation of the RMSEs of the predictors generated for different (s, t) pairs is also measured. Both of these are measured in dBs. In Table 5.2, a comparison of the best NN to GPR and SVM is shown. NN outperforms the other regression methods in terms of RMSE.

Algorithm	NN	GPR	SVM
RMSE	1.41	1.53	1.68
std (RMSE)	0.26	0.16	0.20

Table 5.2: Performance comparison for the whole network; a data set of 5000 users in the 10 cells

In the full network simulation, the data set for learning the SNR prediction function was rather limited. For an ordered pair (s, t) on average some 550 UE locations are sampled. Already with this limited training set, NN outperforms the other predictors. To further clarify the merits of the considered predictors, we construct a larger data set for a pair of cells. We drop a large number of UEs in the street where BSs 1 and 2 are located, and select at random a set of 7000 UE positions that belong to $\mathcal{G}_1^{(2)}$. Channel charting is performed based on the CSI of these UEs, as measured at BS 1, and the CC is annotated with the SNRs of BSs 1 and 2.
A sample of BS $s = 1$ predicting the SNR of $t = 2$ is depicted in Figures 5.14 and Figure 5.15. Figure 5.14 shows the ground truth and predicted BS 2 SNR values in dB, plotted against the ground truth locations. Figure 5.15, in contrast, shows the same ground truth and predicted SNR values, plotted against the CC locations $\mathbf{z} \in \mathcal{C}_s^{(t)}$, which are used as input for predictor

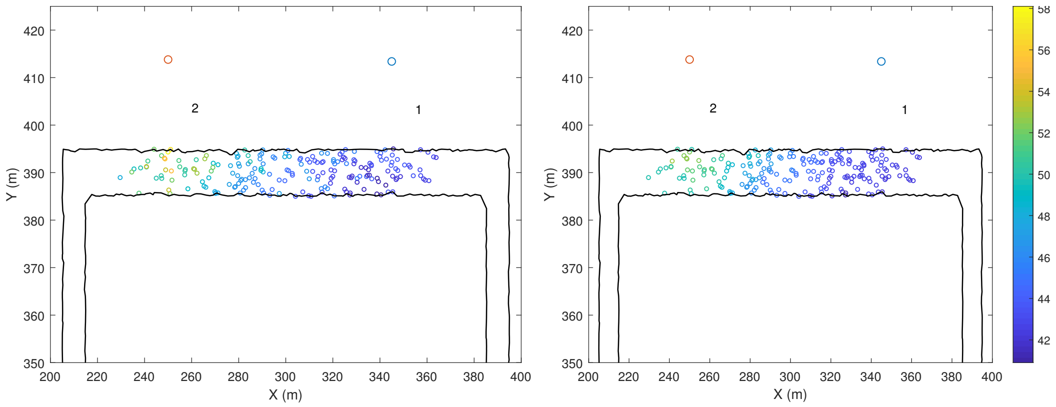

Figure 5.14: Target BS SNR as function of ground truth location. BS 1 & 2 locations marked. Left: Ground truth SNR. Right: Predicted SNR.

training. In addition, an approximate cell boundary is drawn, to sketch the place where BS 2 becomes better than BS 1.

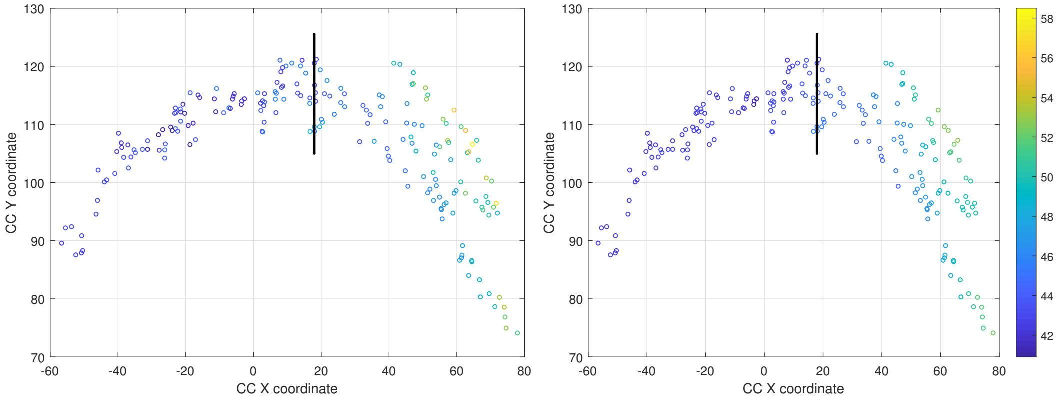

Figure 5.15: Target BS SNR as function of CC location (arbitrary length scale). Left: Ground truth SNR. Right: Predicted SNR. Approximative cell boundary drawn.

For HO, between cells *s* and *t*, the crucial variable to control is the ratio of the SNRs γ_s and γ_t, or their dB-domain difference $\gamma_s - \gamma_t$. Figure 5.16 plots the predicted SNR difference against the ground truth for $s = 1$, $t = 2$, with prediction based on GPR. Similarly, Figure 5.16 shows the predicted SNR difference based on a NN with structure [10 10 10], against the ground truth.
In addition, the 95% confidence interval for the SNR difference prediction using GPR is plotted in Figure 5.17. Interestingly, the edge of NN against GPR seems to arise in the domain where γ_1 is comparable or larger than γ_2, while for γ_2 much larger than γ_1, the algorithms perform similarly. This is encouraging for the prospect of using an NN-based SNR predictor for CCNCH, as the ideal handover location would be $\gamma_2 = \gamma_1$, and this border would be approached from a direction where $\gamma_1 > \gamma_2$.

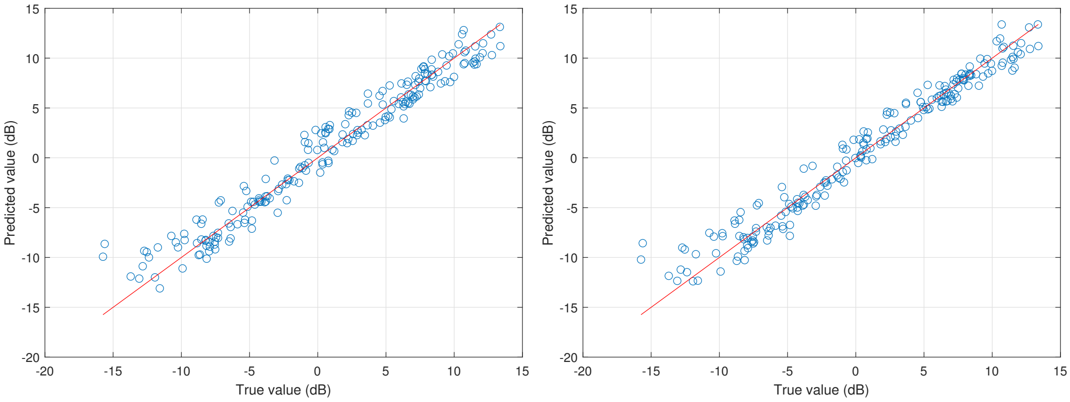

Figure 5.16: Predicted $\gamma_{1,k} - \gamma_{2,k}$ value vs ground truth for Right: NN predictor. Left: GPR predictor.

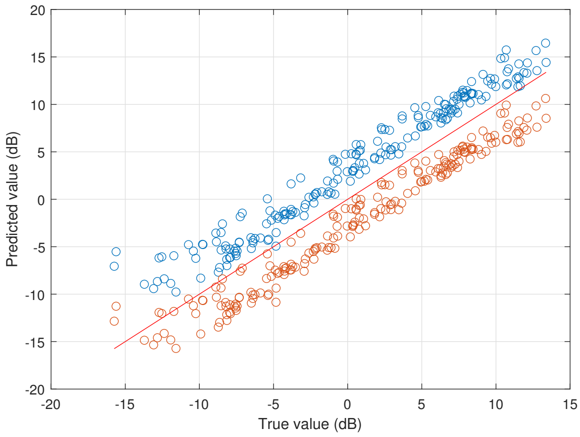

Figure 5.17: Upper and lower bounds of the 95% confidence intervals for predicted value of $\gamma_{1,k} - \gamma_{2,k}$ vs. ground truth using GPR predictor.

6. Conclusion

This deliverable is focused on mm-Wave channel models for 5G and B5G communication systems. Since channel models have a large impact on various aspects of wireless systems ranging from system design to performance analysis, it is critical to develop accurate channel simulators to generate realistic channel responses especially to be used with machine learning algorithms. In this sense, we have presented the role and importance of synthetic data generation in wireless communications. We presented different applications of machine learning to wireless communication that need large synthetic data sets, and characterized their requirements. CC, which is a dimensional reduction of multiuser radio channel features measured at the serving BS, can be applied for radio resource management in future wireless communication systems. In the context of collaborative machine learning, simulators and statistical models represent efficient tools to fabricate training data sets, allowing to avoid burdensome and potentially dangerous real world data collection procedures. Versatility of synthetic data generation procedures has been showcased in the context of distributed power control where the performance of data-driven policies can be easily analyzed under different channel state qualities at transmitters. In the context of Large Intelligent Surfaces, ray-tracing arises as a powerful tool to model the radio propagation environment. In general, it is cumbersome to obtain an analytical solution for the EM field in a realistic scenario. Then, the purpose of ray-tracing propagation modeling is to acquire an estimation of the field/signal strengths in a realistic manner, taking into account physical phenomena such as scattering and diffraction. In this way, ray-tracing is a useful procedure for generating synthetic data that captures both the small and large scale effects of the radio propagation environment as well as the spatial consistency. Besides the potential for high throughput and efficient multiplexing of wireless links, a LIS can offer a high-resolution rendering of the propagation environment. This is because, in an indoor setting, it can be placed in proximity to the sensed phenomena, while the high resolution is offered by densely spaced tiny antennas deployed over a large area.

General frameworks of radio channel models were discussed. Different MIMO channel modeling approaches have been detailed for ease of understanding. The key differences between sub 6 GHz and mm-Wave frequencies such as pathloss, penetration loss, attenuation, channel sparsity, and spatial consistency were explained. Spatial consistency in mm-Wave channel models is an important characteristic the disregarding of which hinders reliable investigation of ,e.g., machine learning tasks which consider channel prediction. The problem of designing spatial consistent large scale measurements at the base station was presented.

Two channel simulators, the QuaDRiGa a ray-tracing based model were presented. Their underlying channel models, layout and system specification, outputs, and applications were discussed. For the QuaDRiGa simulator, spatial consistency of the generated channels in mm-Wave band was investigated and evaluated using different measures. We have analyzed the covariance matrix measured at the BS from the transmission of UE pilot beamformers in terms of the contributions from MPC clusters in mm-Wave channels. As a consequence of MPC clustering, channel covariance has a non-Kronecker structure, and the covariance matrix estimated across time depends on the movement direction. Based on this, we have formulated the UE pilot beamformer selection problem as an optimization problem aiming to preserve spatial consistency of a set of UEs moving in the same large-scale radio environment. We have evaluated the average pairwise CMD for covariance/instantaneous CSI based UE pilot beamformers with different ranks. Simulation results using the QuaDRiGa simulator and 3GPP model have showed that in the absence of noise, the average pairwise CMD distance decreases uniformly with rank.

When discussing the ray-tracing simulator, the underlying mathematical channel model was presented. Sub-ray generation following 3GPP procedures is detailed. The mm-Wave channel model for an urban area (Manhattan grid) is parameterized. We have shown that the relevant clusters in an environment could be geometrically found using ray-tracing channel model. The resulting channel model is useful in assessing the feasibility of mm-Wave communications in urban areas. To determine this, we used the generated channels in a handover detection scenario. We have considered an algorithm for learning the SNR of a user in a neighboring cell from the signal received in a serving cell. The learning is based on a channel chart. A handover algorithm can be designed based on the predicted SNR of the target BS. Three different regression learners have been considered for SNR prediction; Gaussian Process Regression, Support Vector Machines, and Neural Networks. Performance of each learner is evaluated based on RMSE.

Based on the discussion of the channel models, and the evaluations, we conclude that both Quadriga, and the ray-tracing simulator, can be used as channel modeling tools when considering wireless machine learning tasks requiring spatial consistency, as , for example, in the problems addressed in sections 1.1 and 1.3 in this report, which will be investigated in this WP.

7. References

[1] Innovative Training Networks, "Integrating wireless communication engineering and machine learning (WindMill)."

[2] C. Studer, S. Medjkouh, E. Gonultaş, T. Goldstein, and O. Tirkkonen, "Channel charting: Locating users within the radio environment using channel state information," *IEEE Access*, vol. 6, pp. 47682–47698, 2018.

[3] A. Prasad, O. Tirkkonen, P. Lundén, O. N. C. Yilmaz, L. Dalsgaard, and C. Wijting, "Energy-efficient inter-frequency small cell discovery techniques for lte-advanced heterogeneous network deployments," *IEEE Communications Magazine*, vol. 51, no. 5, pp. 72–81, 2013.

[4] J. Deng, S. Medjkouh, N. Malm, O. Tirkkonen, and C. Studer, "Multipoint channel charting for wireless networks," in *Proceedings of 52nd Asilomar Conference on Signals, Systems, and Computers*, pp. 286–290, 2018.

[5] H. Al-Tous, T. Ponnada, C. Studer, and O. Tirkkonen, "Multipoint channel charting-based radio resource management for V2V communications," *EURASIP J. Wireless Comm. and Networking*, vol. 2020, no. 1, p. 132, 2020.

[6] E. G. Larsson, O. Edfors, F. Tufvesson, and T. L. Marzetta, "Massive MIMO for next generation wireless systems," *IEEE communications magazine*, vol. 52, no. 2, pp. 186–195, 2014.

[7] C. Huang, S. Hu, G. C. Alexandropoulos, A. Zappone, C. Yuen, R. Zhang, M. Di Renzo, and M. Debbah, "Holographic MIMO surfaces for 6G wireless networks: Opportunities, challenges, and trends," *IEEE Wireless Communications*, pp. 1–8, 2020.

[8] R. Syms, "Practical volume holography clarendon," *Oxford*, vol. 19902, p. 125, 1990.

[9] T. Rappaport, R. Heath, R. Daniels, and J. Murdock, *Millimeter wave wireless communications*. Prentice Hall, 2015.

[10] S. Arikawa and Y. Karasawa, "A simplified MIMO channel characteristics evaluation scheme based on ray tracing and its application to indoor radio systems," *IEEE Antennas Wireless Propag. Lett.*, vol. 13, pp. 1737–1740, 2014.

[11] O. Stabler and R. Hoppe, "MIMO channel capacity computed with 3D ray tracing model," in *Proceedings of 3rd Europ. Conf. Antennas and Propag.*, pp. 2271–2275, IEEE, 2009.

[12] C. J. Vaca-Rubio, P. Ramirez-Espinosa, R. J. Williams, K. Kansanen, Z.-H. Tan, E. de Carvalho, and P. Popovski, "A primer on large intelligent surface (LIS) for wireless sensing in an industrial setting," *arXiv preprint arXiv:2006.06563*, 2020.

[13] T. S. Rappaport, Y. Xing, G. R. MacCartney, A. F. Molisch, E. Mellios, and J. Zhang, "Overview of millimeter wave communications for fifth-generation (5G) wireless networks—with a focus on propagation models," *IEEE Transactions on Antennas and Propagation*, vol. 65, no. 12, pp. 6213–6230, 2017.

[14] 3GPP, "Study on channel model for frequencies from 0.5 to 100 GHz," TR 38.901, 3rd Generation Partnership Project (3GPP), Dec. 2017. Version 14.3.0.

[15] A. Goldsmith, *Wireless communications*. Cambridge university press, 2005.

[16] S. Sun, T. S. Rappaport, M. Shafi, P. Tang, J. Zhang, and P. J. Smith, "Propagation models and performance evaluation for 5G millimeter-wave bands," *IEEE Transactions on Vehicular Technology*, vol. 67, no. 9, pp. 8422–8439, 2018.

[17] C. R. Anderson, T. S. Rappaport, K. Bae, A. Verstak, N. Ramakrishnan, W. H. Tranter, C. A. Shaffer, and L. T. Watson, "In-building wideband multipath characteristics at 2.5 and 60 GHz," in *Proceedings of IEEE 56th Vehicular Technology Conference*, vol. 1, pp. 97–101 vol.1, 2002.

[18] E. Ben-Dor, T. S. Rappaport, Y. Qiao, and S. J. Lauffenburger, "Millimeter-wave 60 GHz outdoor and vehicle aoa propagation measurements using a broadband channel sounder," in *Proceedings of IEEE Global Telecommunications Conference - GLOBECOM 2011*, pp. 1–6, 2011.

[19] G. R. MacCartney and T. S. Rappaport, "Rural macrocell path loss models for millimeter wave wireless communications," *IEEE Journal on Selected Areas in Communications*, vol. 35, no. 7, pp. 1663–1677, 2017.

[20] S. Sun, G. R. MacCartney, and T. S. Rappaport, "Millimeter-wave distance-dependent large-scale propagation measurements and path loss models for outdoor and indoor 5G systems," in *Proceedings of 10th European Conference on Antennas and Propagation (EuCAP)*, pp. 1–5, 2016.

[21] H. Tataria and F. Tufvesson, "Impact of spatially consistent channels on digital beamforming for millimeter-wave systems," *arXiv preprint arXiv:2003.01653*, 2020.

[22] P. Almers, E. Bonek, A. Burr, N. Czink, M. Debbah, V. Degli-Esposti, H. Hofstetter, P. Kyösti, D. Laurenson, G. Matz, *et al.*, "Survey of channel and radio propagation models for wireless mimo systems," *EURASIP Journal on Wireless Communications and Networking*, vol. 2007, no. 1, 2007.

[23] C. Anioke, C. Nnamani, and C. Ani, "Review of wireless MIMO channel models," *Nigerian Journal of Technology*, vol. 35, no. 2, pp. 381–391, 2016.

[24] M. Patzold and J. A. Hogstad, "A space-time channel simulator for mimo channels based on the geometrical one-ring scattering model," in *Proceedings of IEEE 60th Vehicular Technology Conference, 2004. VTC2004-Fall. 2004*, vol. 1, pp. 144–149 Vol. 1, 2004.

[25] M. Lecci, M. Polese, C. Lai, J. Wang, C. Gentile, N. Golmie, and M. Zorzi, "Quasi-deterministic channel model for mmwaves: Mathematical formalization and validation," *arXiv preprint arXiv:2006.01235*, 2020.

[26] J. W. Wallace and M. A. Jensen, "Modeling the indoor MIMO wireless channel," *IEEE Transactions on Antennas and Propagation*, vol. 50, no. 5, pp. 591–599, 2002.

[27] M. Debbah and R. R. Muller, "MIMO channel modeling and the principle of maximum entropy," *IEEE Transactions on Information Theory*, vol. 51, no. 5, pp. 1667–1690, 2005.

[28] A. G. Burr, "Capacity bounds and estimates for the finite scatterers MIMO wireless channel," *IEEE Journal on Selected Areas in Communications*, vol. 21, no. 5, pp. 812–818, 2003.

[29] J. P. Kermoal, L. Schumacher, K. I. Pedersen, P. E. Mogensen, and F. Frederiksen, "A stochastic MIMO radio channel model with experimental validation," *IEEE Journal on Selected Areas in Communications*, vol. 20, no. 6, pp. 1211–1226, 2002.

[30] W. Weichselberger, M. Herdin, H. Ozcelik, and E. Bonek, "A stochastic MIMO channel model with joint correlation of both link ends," *IEEE Trans. Wireless Commun.*, vol. 5, pp. 90–100, Jan. 2006.

[31] M. Akdeniz, Y. Liu, M. Samimi, S. Sun, S. Rangan, T. Rappaport, and E. Erkip, "Millimeter wave channel modeling and cellular capacity evaluation," *IEEE J. Sel. Areas Commun.*, vol. 32, pp. 1164–1179, June 2014.

[32] F. Wen, H. Wymeersch, B. Peng, W. P. Tay, H. C. So, and D. Yang, "A survey on 5G massive MIMO localization," *Digital Signal Processing*, vol. 94, pp. 21–28, 2019.

[33] Ganame, Yingzhuang, Ghazzai, and Kamissoko, "5G base station deployment perspectives in millimeter wave frequencies using meta-heuristic algorithms," *Electronics*, vol. 8, Nov 2019.

[34] 3GPP, "Study on new radio access technology physical layer aspects," TR 38.802, 3rd Generation Partnership Project (3GPP), Sept. 2017. Version 14.2.0.

[35] D. E. Berraki, S. M. D. Armour, and A. R. Nix, "Application of compressive sensing in sparse spatial channel recovery for beamforming in mmwave outdoor systems," in *Proceedings of IEEE Wireless Communications and Networking Conference (WCNC)*, pp. 887–892, 2014.

[36] G. J. Foschini, "Layered space-time architecture for wireless communication in a fading environment when using multi-element antennas," *Bell Labs Technical Journal*, vol. 1, no. 2, pp. 41–59, 1996.

[37] J. Zhang, X. Ge, Q. Li, M. Guizani, and Y. Zhang, "5G millimeter-wave antenna array: Design and challenges," *IEEE Wireless Communications*, vol. 24, no. 2, pp. 106–112, 2017.

[38] H. Zhao, R. Mayzus, S. Sun, M. Samimi, J. K. Schulz, Y. Azar, K. Wang, G. N. Wong, F. Gutierrez, and T. S. Rappaport, "28 GHz millimeter wave cellular communication measurements for reflection and penetration loss in and around buildings in New York city," in *Proceedings of IEEE International Conference on Communications (ICC)*, pp. 5163–5167, 2013.

[39] J. Ko, Y. Cho, S. Hur, T. Kim, J. Park, A. F. Molisch, K. Haneda, M. Peter, D. Park, and D. Cho, "Millimeter-wave channel measurements and analysis for statistical spatial channel model in in-building and urban environments at 28 GHz," *IEEE Transactions on Wireless Communications*, vol. 16, no. 9, pp. 5853–5868, 2017.

[40] S. Rangan, T. S. Rappaport, and E. Erkip, "Millimeter-wave cellular wireless networks: Potentials and challenges," *Proceedings of the IEEE*, vol. 102, no. 3, pp. 366–385, 2014.

[41] Y. Zeng and R. Zhang, "Millimeter wave MIMO with lens antenna array: A new path division multiplexing paradigm," *IEEE Transactions on Communications*, vol. 64, no. 4, pp. 1557–1571, 2016.

[42] M. Kurras, S. Dai, S. Jaeckel, and L. Thiele, "Evaluation of the spatial consistency feature in the 3GPP geometry-based stochastic channel model," in *Proceedings of IEEE Wireless Communications and Networking Conference (WCNC)*, pp. 1–6, 2019.

[43] H. Al-Tous, P. Kazemi, and O. Tirkkonen, "Coordinated uplink precoding for spatially consistent mmwave channel covariance measurements," in *Proceedings of IEEE 21st International Workshop on Signal Processing Advances in Wireless Communications (SPAWC)*, pp. 1–5, 2020.

[44] R. Wang, C. U. Bas, S. Sangodoyin, S. Hur, J. Park, J. Zhang, and A. F. Molisch, "Stationarity region of mm-wave channel based on outdoor microcellular measurements at 28 GHz," in *Proceedings of IEEE Military Communications Conference (MILCOM)*, pp. 782–787, 2017.

[45] M. K. Samimi and T. S. Rappaport, "3-D millimeter-wave statistical channel model for 5G wireless system design," *IEEE Transactions on Microwave Theory and Techniques*, vol. 64, no. 7, pp. 2207–2225, 2016.

[46] METIS2020, "METIS channel model," Tech. Rep, METIS2020, July 2015. Deliverable D1.4 v3.

[47] L. Liu, C. Oestges, J. Poutanen, K. Haneda, P. Vainikainen, F. Quitin, F. Tufvesson, and P. D. Doncker, "The cost 2100 MIMO channel model," *IEEE Wireless Communications*, vol. 19, no. 6, pp. 92–99, 2012.

[48] T. S. Rappaport, S. Sun, R. Mayzus, H. Zhao, Y. Azar, K. Wang, G. N. Wong, J. K. Schulz, M. Samimi, and F. Gutierrez, "Millimeter wave mobile communications for 5G cellular: It will work!," *IEEE Access*, vol. 1, pp. 335–349, 2013.

[49] T. S. Rappaport, G. R. MacCartney, M. K. Samimi, and S. Sun, “Wideband millimeter-wave propagation measurements and channel models for future wireless communication system design,” *IEEE Transactions on Communications*, vol. 63, no. 9, pp. 3029–3056, 2015.

[50] MiWEBA, “Channel modeling and characterization,” Tech. Rep, MiWEBA, June 2014. Deliverable D5.1.

[51] S. Jaeckel, L. Raschkowski, K. Borner, and L. Thiele, “QuaDRiGa: A 3-D multi-cell channel model with time evolution for enabling virtual field trials,” *IEEE Trans. Antennas Propag.*, vol. 62, pp. 3242–3256, June 2014.

[52] Zhenyu Wang, E. K. Tameh, and A. R. Nix, “A sum-of-sinusoids based simulation model for the joint shadowing process in urban peer-to-peer radio channels,” in *Proceedings of IEEE 62nd Vehicular Technology Conference, 2005.*, vol. 3, pp. 1732–1736, 2005.

[53] A. Corucci, P. Usai, A. Monorchio, and G. Manara, *Wireless Propagation Modeling by Using Ray-Tracing*. "New York NY": Springer New York, 2014.

[54] T. A. Thomas, H. C. Nguyen, G. R. MacCartney, and T. S. Rappaport, “3D mmwave channel model proposal,” in *Proceedings of IEEE 80th Vehicular Technology Conference (VTC2014-Fall)*, pp. 1–6, 2014.

[55] S. Hur, S. Baek, B. Kim, J. Park, A. F. Molisch, K. Haneda, and M. Peter, “28 GHz channel modeling using 3D ray-tracing in urban environments,” in *Proceedings of 9th European Conference on Antennas and Propagation (EuCAP)*, pp. 1–5, 2015.

[56] Y. Chang, S. Baek, S. Hur, Y. Mok, and Y. Lee, “A novel dual-slope mm-wave channel model based on 3D ray-tracing in urban environments,” in *Proceedings of IEEE 25th Annual International Symposium on Personal, Indoor, and Mobile Radio Communication (PIMRC)*, pp. 222–226, 2014.

[57] T. Ponnada, H. Al-Tous, O. Tirkkonen, and C. Studer, “An out-of-sample extension for wireless multipoint channel charting,” in *Proc. of 14th EAI International Conference on Cognitive Radio Oriented Wireless Networks, (Crowncom)*, June 2019.

[58] G. P. Pollini, “Trends in handover design,” *IEEE Commun. Mag.*, vol. 34, pp. 82–90, Mar. 1996.

www.windmill-itn.eu